Nanoscale

REVIEW

View Article Online
View Journal | View Issue

Cite this: *Nanoscale*, 2025, **17**, 17881

2D material-based infrared photodetectors: recent progress, challenges, and perspectives

Muhammad Wajid Zulfiqar, †[a,b,d] Sobia Nisar,†[c,d] Ghulam Dastgeer, *[e] Muhammad Rabeel,[c,d] Hammad Ghazanfar,[a,d] Awais Ali,[f] Muhammad Imran, [g] Honggyun Kim[a] and Deok-kee Kim *[a,c,d]

Infrared (IR) photodetectors are essential for a wide range of applications, including optical communication, night vision, and environmental monitoring. The advent of 2D materials, which have distinctive layered atomic structures, has opened up new possibilities in the fields of electronics and optoelectronics. Rapid progress regarding developing IR photodetectors that are based on 2D materials highlights their potential to revolutionize this technology. This review comprehensively explores recent advancements in infrared (IR) photodetectors that utilize 2D materials and their van der Waals (vdW) heterostructures to analyze the different detection mechanisms that are employed in IR photodetectors. The review also addresses the crucial performance parameters that define photodetector effectiveness, including responsivity, specific detectivity, and noise characteristics. The various applications of IR photodetectors are also explained, including shortwave infrared light detection for medical imaging, infrared multispectral imaging and high frequency and ultra-fast infrared detection. Furthermore, the review discusses the challenges and future outlook for material and device optimization, which includes strategies for hybrid material integration, noise characterization, and scalable production. By examining key performance metrics and comparing various 2D materials, this review aims to offer a blueprint for advancing infrared photodetection research and development, which ultimately paves the way for low-cost, high-performance, and scalable IR sensing technologies.

Received 11th May 2025,
Accepted 7th July 2025

DOI: 10.1039/d5nr01920f

rsc.li/nanoscale

1. Introduction

The emergence of next-generation two-dimensional (2D) materials has transformed the landscape of infrared photodetectors, unlocking unprecedented opportunities for advanced sensing and detection technologies.[1,2] These detectors, particularly those sensitive to wavelengths ranging from 760 nanometers (nm) to 1 millimeter (mm), have attracted a significant amount of research interest in recent decades due to their widespread use in remote sensing, security, environmental monitoring, optical communication, and thermal and medical imaging applications.[3,4] 2D materials offer unparalleled electronic and optoelectronic capabilities, which enable them to achieve remarkable performances in infrared photodetection, such as ultrahigh photoresponsivity, ultrafast response times, broad spectral detection ranges, and exceptional sensitivity.[5,6] 2D materials are unique because they consist of tightly bound atoms that are arranged in a single atomic sheet with strong covalent or ionic bonds. These ultra-thin sheets assemble into layered structures held together by weak van der Waals (vdW) interactions.[7–9] This weak interlayer interaction enables the exfoliation of bulk crystals; that isolates individual flakes or even single atomic layers for various applications. Photodetectors are devices that convert incident electromagnetic radiation into an electric current. 2D materials are revolutionizing photodetector designs due to their unique properties and characteristics. They offer an exceptionally broad spectral response, which detects light from ultraviolet wavelengths to terahertz frequencies (THz). 2D materials also exhibit exceptional photoresponsivity by efficiently converting light into electrical signals.[10] Their versatility extends to polarization-sensitive detection, high-speed response times, and high-resolution imaging capabilities, which makes them ideal for

[a]*Department of Semiconductor Systems Engineering, Sejong University, Seoul 05006, Republic of Korea. E-mail: deokkeekim@sejong.ac.kr*
[b]*Department of Optical Engineering, Sejong University, Seoul 05006, Republic of Korea*
[c]*Department of Electrical Engineering, Sejong University, Seoul 05006, Republic of Korea*
[d]*Department of Convergence Engineering for Intelligent Drone, Sejong University, Seoul, 05006, Republic of Korea*
[e]*Department of Physics and Astronomy, Sejong University, Seoul 05006, Republic of Korea. E-mail: gdastgeer@sejong.ac.kr*
[f]*Department of Materials Science and Engineering, Korea University, 145 Anam-ro, Seongbuk-gu, Seoul 02841, Republic of Korea*
[g]*Department of Chemistry, Faculty of Science, King Khalid University, P.O. Box 960, Abha, 61421, Saudi Arabia*
†These authors contributed equally to the paper.

diverse applications. These heterostructure-based photodetectors demonstrate significant performance enhancements, such as $MoTe_2$–$PdSe_2$ [11] and BP/WS_2 [12] devices, which achieve an exceptionally high rectification ratio, responsivity, and photovoltaic external quantum efficiency (EQE) of 2.6×10^4, 500 mA W^{-1}, and 103%, respectively.

Electrochemical-based infrared (IR) devices represent a promising class of sensors that utilize redox reactions and ion migration to modulate their optical and electrical responses to infrared radiation. These devices incorporate electrochromic materials, solid electrolytes, and ionically active interfaces that undergo a reversible change in their optical and electrical properties upon electrochemical stimulation.[13] Unlike conventional IR detectors, where photon absorption directly generates electron–hole pairs, these devices utilize photoelectrochemical processes where a change in local electrochemical environment influences charge transport and light absorption properties. These photogenerated carriers modulate redox reactions at the electrode–electrolyte interface, resulting in current (amperometric), voltage (potentiometric), and impedance (impedimetric) changes that can be detected as IR signals. Electrochemical IR devices offer several benefits, including low power requirements, adjustable response characteristics, mechanical flexibility, and compatibility with transparent and stretchable substrates. These characteristics make them highly suitable for advanced applications such as wearable electronics, adaptive optical systems, and neuromorphic sensing, where real-time and tunable IR detection is critical.[14,15]

The ISO 20473 standard divides infrared radiation into three regions based on wavelength, namely, near-infrared (NIR) from 0.78 to 3.0 micrometers (μm), mid-infrared (MIR) from 3.0 to 50 μm, and far-infrared (FIR) from 50 μm to 1 mm.[16] Around half of the sun's energy reaches us in the form of NIR light. This abundance highlights the importance of developing materials that can absorb and convert this NIR light into electricity using photovoltaic cells. NIR sensing, detection, and monitoring have significant advantages over traditional methods due to NIR light's unique properties. For instance, NIR light can penetrate deeper into biological tissues compared to visible light, which makes it suitable for medical applications. The evolution of NIR technology has enabled the development of NIR detectors with remarkable sensitivity. NIR detectors are broadly categorized into three main types based on their detection mechanisms: thermal detectors, photoconductive detectors, and avalanche photodiodes (APDs). Thermal detectors measure temperature changes that are caused by absorbed NIR radiation, and they convert these changes into electrical signals. Photon detectors, which include photoconductive detectors and APDs, directly detect photons and convert them into an electric current through the photoelectric effect. Photoconductive detectors generate electron–hole pairs in semiconductors upon photon absorption, which alters their electrical conductivity. APDs, under a high electric field, amplify this initial signal *via* an avalanche multiplication process and provide extremely high detectivity and sensitivity. Recent advancements in nanoscience and nanotechnology have significantly reduced the size of NIR devices in the past decade. NIR devices that utilize low-dimensional semiconductor nanostructures, which include one-dimensional (1D) structures, such as nanowires (NWs), nanorods (NRs), and nanobelts (NBs), offer several key advantages, such as high detectivity, responsivity and ON/OFF ratio, minimum energy usage, and flexible integration into devices, compared to traditional NIR devices that are made from bulk materials or thin films.

The phenomenon behind the high responsivity and detectivity in 1D nanostructures is due to reduced dimensionality and a large surface-to-volume ratio, which lead to shorter transit times. 1D nanostructures have a significantly larger surface area relative to their volume compared to bulk materials. This increased surface area potentially introduces more surface trap states, which temporarily capture photogenerated carriers, such as electrons and holes, that are created by absorbed NIR light. These traps can potentially act as recombination centers, but they can also extend the lifetime of these photocarriers within the material in some cases. A longer photocarrier lifetime allows for a greater chance for the carriers to contribute to the electrical current before recombining, which ultimately leads to a stronger electrical response. The 1D geometry of these nanostructures confines the movement of the photogenerated carriers within a smaller area than that in bulk materials. This effectively shortens the transit time, the duration required for carriers to travel through the device, and contributes to the current. A shorter transit time translates to faster response times and reduces opportunities for carrier recombination within the material, which further enhances the detector's sensitivity.[17] Mid-infrared (MIR) and far-infrared (FIR) photodetectors hold particular significance for photodetection due to two major advantages: the atmospheric window and thermal information. The MIR spectrum coincides with a natural window in the Earth's atmosphere. This window allows for a significant portion of MIR radiation to pass through with minimal absorption by atmospheric gases. This property makes MIR ideal for applications where long-distance and unobstructed detection of light is crucial, such as remote sensing or free-space optical communication. MIR radiation interacts with the vibrational modes of molecules; this is unlike visible or near-infrared light, which primarily interacts with the electronic structure of molecules. These vibrations are directly linked to the temperature of the object. MIR detectors can therefore provide valuable thermal information, which allows us to detect the presence of an object and remotely estimate its temperature. This capability finds applications in various fields, which include night vision, thermal imaging for security purposes, and non-invasive temperature measurement in medical diagnostics.[18,19]

1.1 Objective of the review

There has been a significant amount of progress in recent years with regard to the development of infrared (IR) detectors using 2D materials, which are distinguished by their unique

electrical and optical characteristics.[20–22] There is a need for a comprehensive analysis that evaluates and compares the various 2D materials and their applications with regard to IR detection, despite numerous studies on specific materials and device topologies. This review seeks to fill this gap by thoroughly examining the various 2D materials that are utilized in IR photodetectors by analyzing their unique features and evaluating the tactics that are adopted in order to improve device performance. Our objective is to offer a clear and detailed overview of the current state of the field, identify the challenges that remain, and propose potential directions for future research, which will thereby guide the continued development of 2D material-based IR photodetectors. It provides an in-depth analysis of the mechanisms, performance metrics, and practical applications of these detectors while evaluating the limitations and gaps in existing research. We begin this

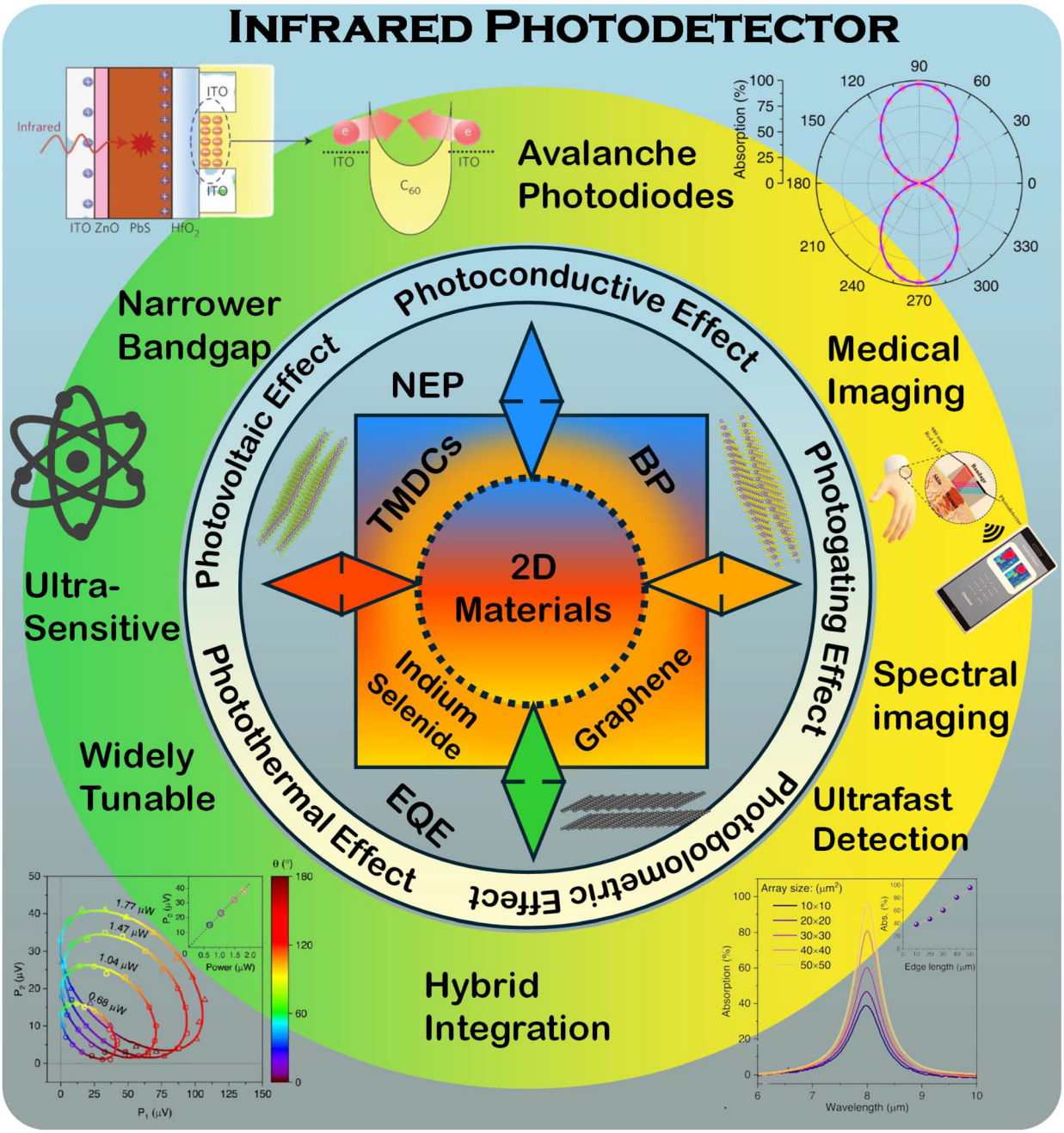

Fig. 1 This work presents a detailed overview of 2D material-based infrared photodetectors and their integration into advanced detection technologies. It highlights the unique optical and electronic properties of 2D materials, which are critical in regard to achieving high sensitivity, tunable detection, and enhanced device performance that holds significant potential for applications in medical imaging, environmental monitoring, and communication systems, and contributes to innovative and scalable solutions for global technological needs.[23–26]

review with a comprehensive overview of the history, detection mechanisms, and classification of IR detectors. The focus then shifts to the unique properties of 2D materials, such as their tunable band gaps, thickness-dependent behavior, and carrier mobility. We discuss how these characteristics influence key detector parameters, such as responsivity, detectivity, EQE, and noise equivalent power (NEP). We explore the exciting possibilities of 2D material-based IR detectors by highlighting their potential for wide tunability, ultra-sensitivity, and suitability for various applications of medical imaging, spectral imaging, and high-frequency devices. We discuss some challenges faced by traditional IR detectors in the closing paragraph. These include the need for cryogenic cooling, limitations due to background noise, and the instability of some materials in the air. This review surveys the recent advancements, challenges, future directions, and general design principles for high-performance photodetectors, which aim to guide the development of next-generation devices. The 2D materials, detection mechanisms, metrics, and application of IR sensing are shown in Fig. 1.

2. History of infrared (IR) photodetectors

The use of heat has been understood for millennia, but the scientific discovery of infrared radiation is a relatively recent event. Astronomer William Herschel conducted a groundbreaking experiment in 1800 that led to the identification of this invisible form of light. Herschel's experiment involved a crude monochromator, which is a device that separates light into its constituent colors. He used a thermometer to measure the temperature changes caused by different colors of sunlight passing through the monochromator. He notably observed a significant temperature increase beyond the visible red spectrum. This observation, which was documented in his notes,[27] confirmed the existence of infrared radiation, which is a type of radiation that is invisible to the human eye but is detectable as heat. The history of infrared (IR) detectors reveals a focus on thermal detection methods. Pioneering advancements include the 1821 invention of the thermocouple, which converts heat to electricity, by Seebeck. Nobili built on this thermopile in 1829 by connecting multiple thermocouples for increased sensitivity. Another thermal detector, Langley's bolometer, emerged in 1880. Langley's design relied on changes to the electrical resistance of thin metal strips exposed to IR radiation. His bolometer eventually detected heat from a distant cow *via* continuous refinement, which demonstrated impressive progress in early IR detection technology.[28–30] Thermal detectors dominated early IR technology, but the 20th century saw the rise of photon detectors. A pioneering study by Case in 1917 led to the first IR photoconductor.[31] Lead sulfide, which was discovered by Kutzscher in 1933, offered a response of up to 3 μm.[32] Norton's observation highlights the vast potential for IR detection, which encompasses various physical phenomena from thermoelectric effects to photon absorption.[33] This diversity continues to drive innovation in regard to IR detector technology.

Semiconductor IR detectors have significant advantages, but their widespread use is hindered by the need for cryogenic cooling. This cooling is necessary because thermal energy can excite electrons in the semiconductor and create unwanted background noise even at room temperature. This noise can overwhelm the weak signal that is generated by IR radiation, which reduces the detector's sensitivity. Cryogenic cooling systems are bulky, expensive, and inconvenient, which limit the portability and practicality of IR systems based on these detectors. New techniques are being analyzed with advancements in device engineering and materials science in order to address these challenges; these include (a) narrower bandgap materials; semiconductor materials with inherently narrower bandgaps enable the detection of longer IR wavelengths at higher operating temperatures. This reduces or eliminates the need for cryogenic cooling for certain IR detection applications.[34,35] (b) Advanced doping techniques; the strategic doping of semiconductors with impurities enables the creation of new energy levels within the bandgap, which influence the electrical conductivity. These levels can enhance the absorption of specific IR wavelengths and improve sensitivity at higher temperatures.[36,37]

There are various categories of semiconductor IR detectors, and each of them has its own operating principles and performance characteristics. Intrinsic detectors rely on the pure semiconductor material for IR absorption and have a broad spectral response, whereas doping introduces additional energy levels within the bandgap in extrinsic detectors, which tailor the detector's response to specific IR wavelengths. Photoemissive detectors utilize the photoelectric effect, where IR radiation ejects electrons directly from the material and generates an electrical current. Quantum well detectors exploit the unique quantum mechanical properties of layered semiconductor structures in order to achieve improved detection capabilities and high sensitivity.

Thermal detectors focus on the heating effect of infrared radiation, which is unlike semiconductor detectors that rely on direct photon absorption. IR radiation gets absorbed when it strikes the detector material, which causes the temperature to rise. This temperature change triggers a shift in the physical properties of the material, such as electrical conductivity, mechanical strain, or even magnetism, depending on the design. This variation in the chosen property is then converted into an electrical output signal. The detector element is typically suspended on heat-resistant supports in order to minimize the environmental influence and ensure it responds primarily to the temperature change that is caused by the absorbed IR radiation. Thermal detectors may have slower response times compared to their semiconductor detectors, but their simpler fabrication process and wide range of detectable wavelengths make them a valuable choice for specific IR sensing applications that prioritize cost-effectiveness and broad spectral responses.[38] Their key advantage lies in their wavelength independence, because it can detect a broad spec-

trum of IR radiation with similar sensitivity, regardless of the specific IR wavelength. The strength of the electrical output signal depends on the total amount of IR radiation absorbed, and it does not depend on the individual photons themselves. The ability to operate at ambient temperatures makes them particularly attractive compared to high-performance photon detectors, which often rely on intricate cooling setups. The core principle behind thermal detectors involves converting a temperature rise, which is caused by IR absorption, into an electrical signal. This conversion can be achieved by measuring changes in electrical resistance (bolometers) or internal material polarization (pyroelectric detectors).

2D semiconductor materials have become a cornerstone of modern IR detection technology by offering significant advantages over traditional thermal detectors. These advantages stem from their unique ability to directly convert absorbed IR radiation into an electrical signal that relies on the fundamental principle of bandgap theory. According to bandgap theory, electrons in a semiconductor material can only occupy specific energy levels within defined bands. The bandgap in materials refers to the energy difference that separates the occupied valence band from the empty conduction band. Individual photons can be absorbed by electrons if the photon's energy precisely matches the bandgap energy when IR radiation interacts with the material. An electron is excited from the valence band to the conduction band when light is absorbed, which creates an electron–hole pair. The hole represents the vacant space that is left in the valence band. The formation of electron–hole pairs influences the electrical properties of the semiconductor. This leads to an increase in the material's electrical conductivity in most cases. This change in conductivity forms the basis for the electrical output signal that is measured by the detector. A key advantage of semiconductor IR detectors is their wavelength selectivity. Different semiconductor materials possess varying band gaps. The detector can be tailored to more efficiently absorb those specific wavelengths by choosing a material with a bandgap that aligns with the desired IR detection range. This targeted absorption translates into a stronger electrical signal for the relevant IR radiation. The absorption of photons and the creation of electron–hole pairs happen quickly at the atomic level; this results in fast response times for these detectors and enables them to detect pulsed infrared signals with high temporal resolution. 2D semiconductor infrared detectors provide a powerful combination of high sensitivity, low noise, fast response times, and wavelength selectivity, which makes them valuable for various infrared sensing applications.[39]

Unlike bulk semiconductors that typically have fixed band gaps, many 2D materials exhibit a layer-dependent band gap.[40–42] Graphene, a zero-bandgap conical structure, inherently offers an ultra-broadband response from the visible to the far-infrared (THz) range due to its dispersion relationship (Dirac cones) and strong light–matter interactions. It can detect infrared (IR) light without the need for an additional absorber due to the relatively high Seebeck coefficient (~40–60 μV K^{-1}), which is significantly greater than that of typical metals and its strong optical absorption in the mid-infrared range (7–17 μm). This is particularly advantageous, as most conventional infrared sensing materials have wide band gaps that limit their ability to absorb IR radiation directly.[43,44] Black phosphorus (BP) possesses a highly tunable direct bandgap, ranging from 0.3 eV in its bulk form to 1.5 eV as a monolayer, enabling efficient light absorption across the short-wave infrared (SWIR) and mid-wave infrared (MWIR) regions, depending on its thickness. This tunability makes BP particularly suitable for mid-infrared detection.[45] By leveraging the Stark effect, BP demonstrates broadband infrared detection from 3.7 to beyond 7.7 μm, with peak extrinsic photoresponsivities of 518, 30, and 2.2 mA W^{-1} at 3.4, 5, and 7.7 μm, respectively, at 77 K. The photocarrier lifetime, with an operational speed of up to 1.3 GHz, enables BP to support high-performance mid-infrared photodetectors with a fast response, broad spectral tunability and high sensitivity.[46,47] Narrow bandgap transition metal dichalcogenides (TMDCs) (*e.g.*, $MoTe_2$, $PtSe_2$, $PdSe_2$) are being explored for MWIR and LWIR detection. For instance, molybdenum ditelluride ($MoTe_2$) has an intrinsically narrower bandgap in the range of 0.8–1.1 eV for its monolayer form and even smaller for the bulk. It exhibits good thermoelectric properties, enabling a photothermoelectric detection mechanism that is inherently broadband and can operate at room temperature. These TMDCs possess relatively high carrier mobilities, which are crucial for a fast photoresponse and efficient charge collection.[48,49]

3. IR detector types

3.1 Classification of IR detectors

Semiconductor detectors dominate infrared (IR) detection technology. These detectors belong to the class of photon detectors where light interacts with electrons in the material, which causes a change in their energy distribution. This change results in a change to an electrical signal. A key advantage of photon detectors is their wavelength-specific response —they only respond to certain infrared wavelengths—which offers an excellent SNR and fast response. However, achieving this performance requires cryogenic cooling.[50,51] Recently, the field of outer atmosphere research has witnessed a growing focus on longer wavelengths due to their potential applications. Photon detectors can be further classified based on the nature of light interacting with the material and the resulting operational mode, which includes intrinsic detection where light interacts directly with the inherent electronic structure of the material. However, the presence of impurities or dopants within the material influences how light interacts and generates a signal in extrinsic detectors. A photoemissive detector relies on the emission of electrons from a metal surface upon light absorption and quantum well detectors where engineered structures are used for quantum confinement effects in order to enhance light detection in specific wavelength ranges.[52] Detectors can be further categorized based on how the electric or magnetic field within the device

facilitates signal generation, regardless of the material system that is used. Light absorption increases the material's conductivity in photoconductive mode, which leads to a change in the current flow through the device. Under photovoltaic operation, incident light generates an internal voltage known as a photovoltage, which results from the separation of electron–hole pairs by an internal electric field. It utilizes the movement of charges within the detector under the influence of light and an applied magnetic field in photoelectromagnetic (PEM) mode. The choice of material for a photon detector plays a crucial role in determining a suitable operational mode. Different material systems can be effectively employed in various operational modes, depending on their properties and the desired detection characteristics.[53,54]

Thermal detectors represent a distinct class of IR detectors that operate based on a different principle than photon detectors. Thermal detectors, which are unlike photon detectors that directly interact with light on an electronic level, focus on the thermal effects of the absorbed infrared radiation. These detectors function by absorbing infrared radiation and converting it into heat, which produces a measurable electrical signal. When NIR radiation is absorbed, the temperature of the detector material rises. In a bolometer, this temperature increase causes the material's electrical resistance to change. Under an applied bias, the resulting variation in current is proportional to the incident NIR power, yielding an electrical output that reflects the absorbed radiation. These detectors are broadly classified into six categories based on their working principles: (a) dielectric bolometers rely on the temperature-dependent dielectric constant of a material to produce a detectable signal;[55] (b) pyroelectric detectors use materials with spontaneous polarization that varies with temperature to produce a voltage;[56] (c) thermoelectric sensors rely on the Seebeck effect where a temperature gradient across a junction of two different conductors produces a voltage;[57] (d) resistive bolometers measure changes in electrical resistance that occur as the detector temperature changes;[58] (e) mechanical displacement devices detect deflection caused by the material's thermal stress when one layer expands more than another under heating;[59] (f) diode-based detectors depend on the temperature sensitivity of a diode's *I–V* characteristics to register changes in absorbed radiation.[60] A schematic of the working principle for thermal IR detection is shown in Fig. 2(a). In a photoconductive detector, incoming NIR photons with sufficient energy promote electrons from the valence band into the conduction band, creating additional charge carriers. Under a small, applied voltage in the dark, only a minimal population of thermally generated carriers is present. Once illuminated, the sudden rise in carrier density lowers the resistance of the material, allowing more current to flow for the same bias. These photogenerated e–h pairs are separated by the electric field where electrons drift towards the negative electrode and holes towards the positive electrode. However, the speed of photoconductive detectors is limited by

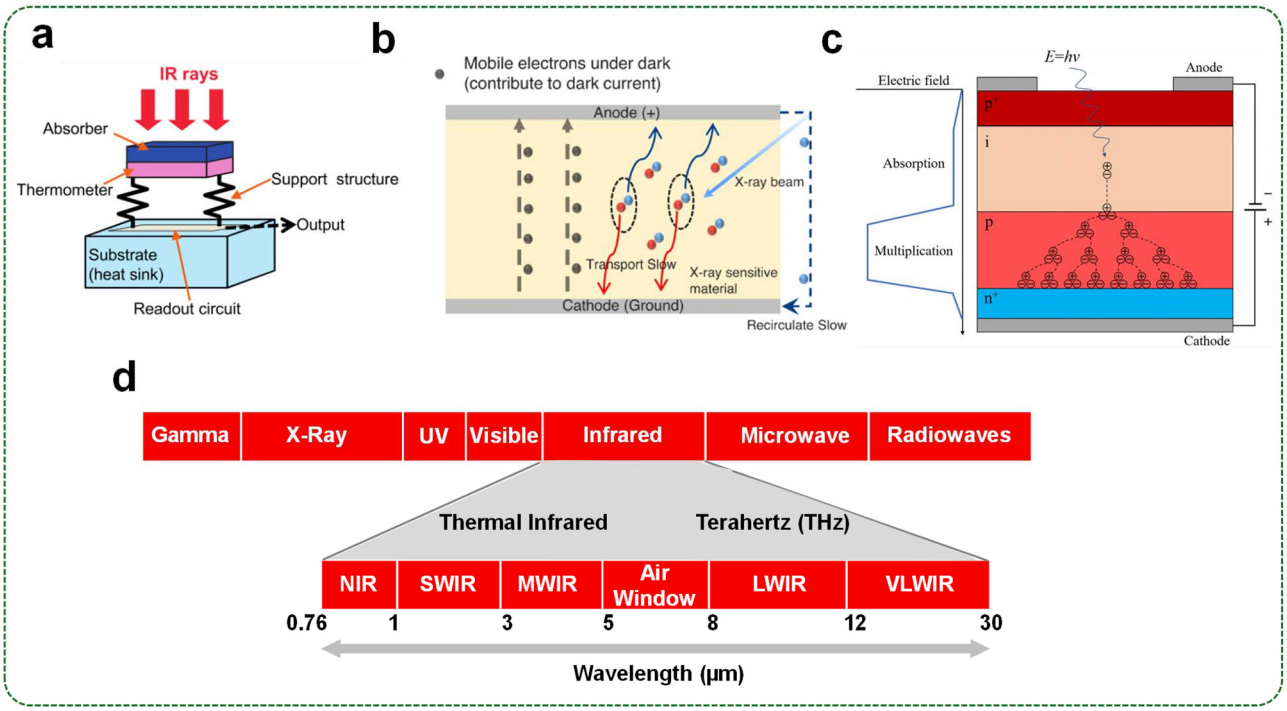

Fig. 2 Classification of IR detectors based on mechanism. (a) Thermal detector where absorbed IR light is converted into heat, which results in a measurable electrical signal, adapted with permission from MDPI.[63] (b) Photoconductive detector where NIR photons promote electrons from V.B. to C.B. and reduce electrical resistance and increase electrical current, adapted with permission from Nature.[64] (c) Avalanche photodiode where internal gain mechanisms generate e–h pairs upon absorption of NIR photons, adapted with permission from Springer Nature.[65] (d) Electromagnetic spectrum highlighting the infrared region, which is subdivided into different regions.

Table 1 A summary of photon and thermal detectors, outlining their advantages and disadvantages

Type		Advantages	Disadvantages
Photon	Intrinsic	Simple preparation and stability	High and large thermal expansion and permittivity
	Extrinsic	Operates over a wide wavelength range and easy to use	Requires very low temperature for operation and high thermal generation
	Free carrier	High yield, low cost	Operates at low temperature and low quantum efficiency
	Quantum wells	Large area growth with uniformity, multi-wavelength detector	High thermal generation and design complications
Thermal		Low cost, reliable and room temperature operation	Slow response and low detectivity at high temperatures

the carrier lifetime and carrier transit time. A thicker layer absorbs more photons but also increases the transit time, which can slow the response. The working principle of the photoconduction detector is shown in Fig. 2(b).

APDs incorporate an internal gain mechanism, generating e–h pairs upon the absorption of IR photons. The internal gain in an APD arises from avalanche multiplication, which begins when the device is biased above the impact-ionization threshold. The electric field within the APD accelerates these initial carriers, which causes them to collide with other atoms and generate additional carriers. This avalanche effect amplifies the weak signal that is generated by the absorbed IR radiation, which leads to improved detection sensitivity even at higher operating temperatures.[61,62] This amplification can potentially reduce or eliminate the need for cryogenic cooling in specific scenarios. The operating principle of an avalanche diode is shown in Fig. 2(c). The electromagnetic (EM) spectrum, where infrared regions are further divided into regions based on their wavelengths, is shown in Fig. 2(d).

An overview of photon and thermal detectors, highlighting their advantages and limitations, is provided in Table 1.

4. Working mechanism of IR photodetectors

An infrared (IR) photodetector detects IR radiation and converts it into an electrical signal. The operating principle typically involves a semiconductor material sensitive to IR wavelengths, where incident IR photons excite electrons from the V. B. into the C.B., creating e–h pairs. These carriers are then driven by an internal or external electric field and generate a photocurrent. We discuss each effect in detail below in order to understand its operation.

4.1 Photoconductive effect (PCE)

It is the widely used mechanism where IR photons with sufficient energy strike the detector material and excite electrons; this causes them to jump into the conduction band from the valence band to generate carriers. These mobile carriers increase the material's electrical conductivity, which results in a measurable photocurrent. The magnitude of this current depends on the number of e–h pairs generated, which is directly related to the incident IR radiation intensity, as shown in Fig. 3(a). In this effect, an external bias is applied to measure changes in conductivity and convert them into a usable electrical signal. An electric field is generated within the material when a potential difference is applied across the source and drain contacts and exerts a force on the free holes and electrons generated by the absorbed IR radiation. This force accelerates these charged particles in opposite directions, which causes them to drift through the material. This directed movement of charges constitutes an electrical current, which is known as the photocurrent. The intensity of the electrical current depends on several factors, such as the applied bias voltage and intrinsic property of the material. There is an optimal bias voltage that balances maximizing the drift velocity of the current with minimizing unwanted effects, such as Joule heating within the material.[66,67] Photons with energies that exceed the material's bandgap are absorbed and excite electrons to the conduction band when IR radiation strikes the detector. An applied voltage bias (V_{ds}) establishes an electric field within the detector. This electric field drives the separation of e–h pairs, which pushes the carriers toward positive and negative electrodes. The resulting flow of the current ($\Delta I = I_{photo} - I_{dark}$) that is attributed to these photogenerated carriers constitutes the photocurrent (I_{photo}), which is the measurable increase in current compared to the dark current (I_{dark}).

Photoconductors typically employ a simple design that consists of a layer or junction of a photoconductive material. This transistor structure utilizes an insulating layer in order to electrically isolate the gate electrode from the underlying semiconductor channel, which enables modulation of the conductivity of the channel without directly injecting current into it, as shown in Fig. 3(b). The back gate helps in regard to maximizing light absorption within the photosensitivity channel, which is unlike the top gates that obstruct the incident light with metal electrodes. The back gate offers electrostatic control over the channel conductivity. The device can deplete unwanted charge carriers that arise from background doping and impurities in the material, which significantly reduce the dark current, by varying the gate voltage. FETs that utilize atomically thin 2D materials, such as TMDCs or graphene, offer an additional advantage. The depletion region that is induced by the back-gate can extend through the entire channel thickness due to their ultra-thin nature.[68] This complete depletion provides superior suppression of the background carriers, which leads to even lower dark currents compared to FETs that are based on bulk semiconductor materials.

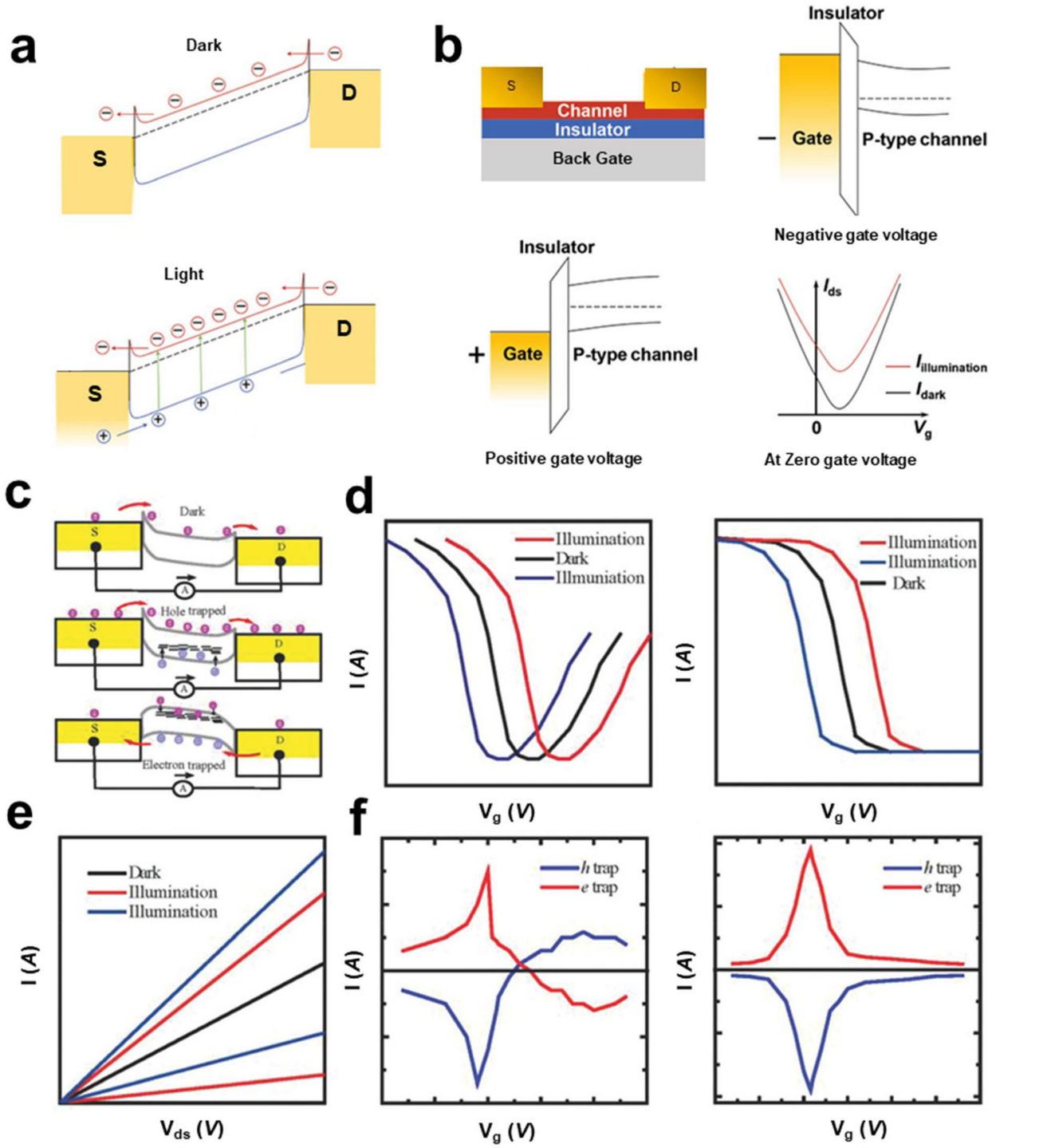

Fig. 3 Schematic representation of an IR detection mechanism with the transfer and *I*–*V* curves for the PCE and PGE. (a) PCE in a semiconductor channel. The upper panel shows a small current under dark conditions, whereas the lower panel under light conditions shows a significant current flow due to the excitation of an additional charge carrier. (b) The upper left panel shows the back gate photodetector, the top right and bottom left panels represent the change in energy levels under different gate voltages, and the bottom right panel illustrates the photocurrent response with and without illumination. (a and b) Adapted with permission from Wiley.[71] (c) The top panel shows the PGE effect under dark conditions with a minimal mobile charge carrier and the device exhibits low conductivity. The middle and bottom panels illustrate holes and electrons that are trapped likely due to defects or impurities in the material. (d) PGE transfer curves for an ambipolar FET that conducts currents under both negative and positive gate voltages and a unipolar FET, which primarily conduct currents in one polarity depending on the design. (e) *I*–*V* curves illustrating the relationship between the current (*I*) and the applied voltage (*V*) under dark conditions and illumination. (f) Photocurrent when a gate voltage is applied for a unipolar and ambipolar FET. The ambipolar photocurrents change sign depending on the gate voltage, because a dominant carrier type can be influenced by the gate voltage. However, it maintains the same sign in a unipolar FET, because the dominant carrier type remains the same, and light-induced conditions primarily affect the number of mobile carriers. (c–f) Adapted with permission from Wiley.[72]

4.2 Photogating effect (PGE)

The photogating effect in phototransistors plays an important role with regard to influencing the detector's performance. This phenomenon arises from the interaction between light-generated carriers and trap states within the device. The phototransistor absorbs photons when exposed to light with energy that is greater than the bandgap. An applied bias voltage source–drain (V_{ds}) across the device separates these photogenerated carriers. Electrons drift towards the drain, whereas holes move towards the source. However, some carriers might encounter trap states within the channel. These trap states, which are often caused by defects or impurities, can capture either electrons or holes. If a significant number of holes become trapped in these states, they create localized regions with positive charges within the channel. These positively charged regions act as a virtual *floating gate*, and they influence the overall channel conductivity *via* electrostatic interactions, which are shown in Fig. 3(c). The presence of trapped holes effectively reduces the number of free holes that are available for conduction, which thereby modulate the channel current. This results in increased responsivity and a lower dark current. Due to the photogating effect, the photocurrent, which is directly proportional to free carriers, becomes highly sensitive to variations in light intensity. The trapped holes can also act as a barrier, which hinders the flow of the thermally generated dark current in the absence of light, which leads to a lower baseline current and a higher signal-to-noise ratio (SNR). Low-dimensional nanomaterials, such as quantum dots (QDs), zero-dimensional (0D) and one-dimensional (1D) nanowires, and 2D materials, exhibit a significant advantage with regard to photogating compared to traditional bulk materials.[69,70] The transfer and *I–V* curves under light and dark conditions are shown in Fig. 3(d and e). These nanomaterials possess an inherently large surface area to volume ratio, and they have a large amount of surface defect states compared to their bulk counterparts. These surface defects often create trap states within the material. Light interacts with the material during photoexcitation, which generates electron–hole pairs. These carriers can become trapped within the abundant surface defect states. This also helps with regard to reducing screening effects, which refer to the ability of free carriers to counteract the electric field that is generated by trapped charges. The presence of a high density of carriers in bulk materials efficiently screens the electric field from trapped charges. This limits the overall influence of trapped charges on the channel conductivity. Low-dimensional materials exhibit weaker screening effects due to their reduced dimensionality and lower carrier density. This enables the electric field that is generated by trapped holes to extend further into the channel, which leads to a more pronounced modulation of the channel conductivity. The stronger modulation of the channel conductivity in low-dimensional materials due to photogating helps with regard to achieving greater sensitivity for photodetectors. Fig. 3(f) shows the photocurrent with a change in the gate voltage (V_g).

4.3 Photobolometric effect (PBE)

Photons with sufficient energy can be absorbed when light strikes the photodetector material. This absorption process excites electrons within the material to higher energy states. These excited electrons lose energy through various mechanisms, which include collisions with other atoms within the material, as they return to their ground state. These collisions result in increased thermal energy, which effectively heats the material. The electrical resistance of a material is intrinsically linked to its temperature. The resistance increases in most materials, because the temperature rises due to the increased scattering of electrons by thermal vibrations within the material, which hinder their ability to flow freely. The light-induced heating results in changing the resistance of the active material in a photobolometric detector.[73,74] This change in resistance can be electronically measured, and it serves as the signal that corresponds to the incident light intensity, which is shown in Fig. 4(a and b). Resistance in a material arises from opposition to the flow of the electric current. This current opposition is primarily due to collisions between charge carriers, such as electrons or holes, and different types of impurities, defects, and thermal vibrations of atoms. The temperature of a material increases when it is exposed to thermal radiation. This temperature rise intensifies the thermal vibrations of the atoms within the material. Thermal irradiation can lead to an increase or decrease in resistance, depending on the material properties, as shown in Fig. 4(c). The increased thermal vibrations usually enhance the scattering of electrons in semiconductors. This increased scattering makes it more difficult for the electrons to move freely through the material and leads to a rise in resistance. Thermal irradiation can have the opposite effect in some metals. Thermal vibrations do increase scattering, but some bound electrons in the metal atoms gain enough thermal energy to break free and become conduction electrons at higher temperatures. This increase in the overall number of carriers can outweigh the increased scattering, which leads to a decrease in resistance. Any absorbed IR radiation is converted into heat, so bolometers exhibit a broad spectral response that can encompass a wide range of IR wavelengths, which include those from mid-wave infrared (MWIR) to terahertz (THz). This broadband detection capability makes bolometers particularly suitable for applications such as space, because it detects faint heat signatures from distant objects over a vast spectral range. Fourier-transform infrared (FTIR) spectroscopy relies on broadband detection with regard to analyzing the chemical composition of materials based on their IR absorption spectra.

4.4 Photothermal effect (PTE)

The photothermal effect (PTE) is a phenomenon where light absorption generates a voltage in a material. This effect arises due to the interplay between light-induced heating and the material's thermoelectric properties, as shown in Fig. 4(d). The Seebeck effect plays a crucial role in the PTE when a temperature difference (ΔT) is established across a material. This occurs when one side of a semiconductor absorbs light and

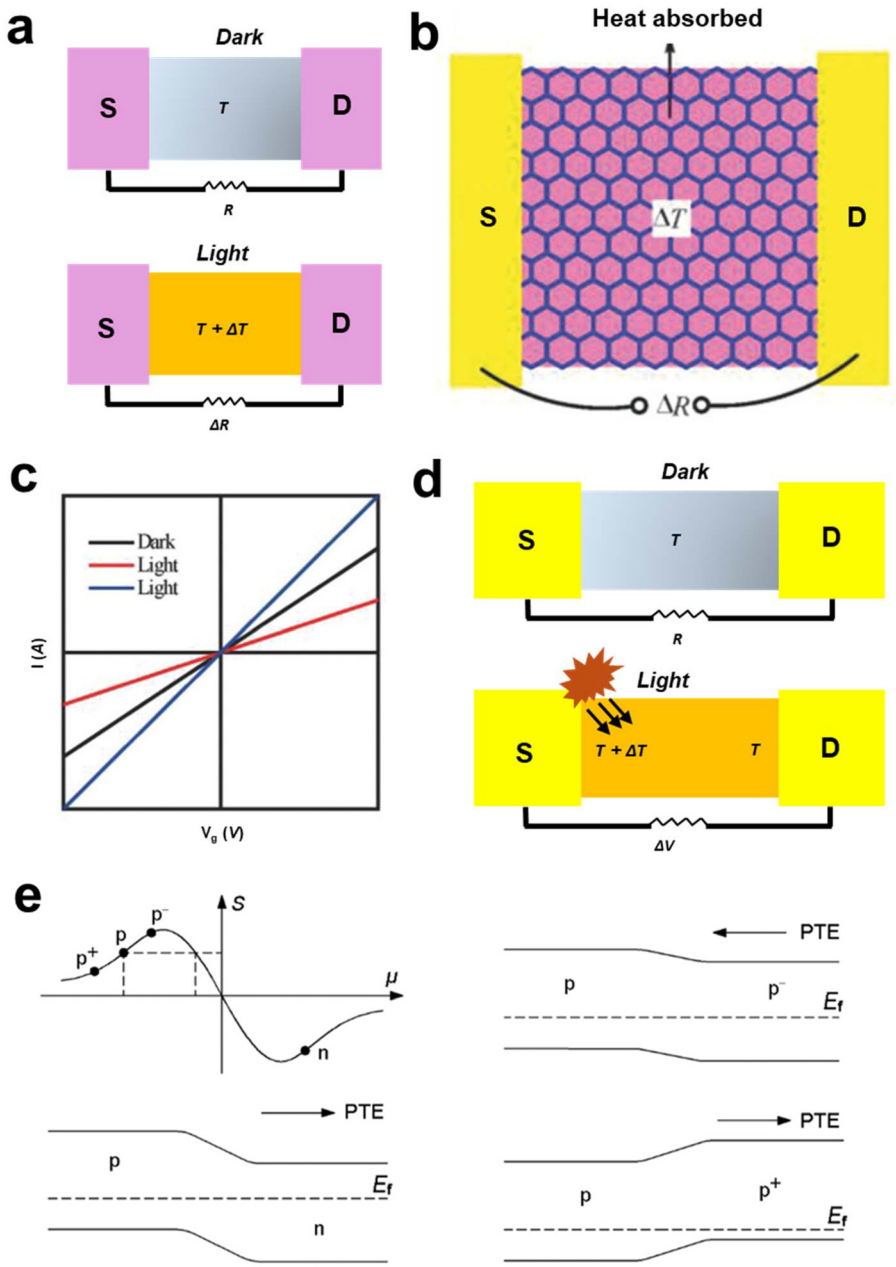

Fig. 4 Schematic of the IR detection mechanism with transfer and *I*–*V* curves for the PBE and the PTE. (a and b) PBE schematic mechanism showing the influence of light on the electrical resistance of the material. The device is at a base temperature (T) that corresponds to resistance (R) under dark conditions. The material absorbs energy, which increases the thermal energy by ΔT, corresponding to ΔR when exposed to light. The atomic vibrations within the material intensify, which makes it more difficult for the electrons to flow freely; as the temperature increases, the atomic vibrations within the material intensify and make it more difficult for electrons to flow freely. (c) *I*–*V* characteristics of PBE. The two curves represent the device's behavior under dark and light conditions. PBE dominated detectors cannot operate at zero bias, unlike some photodetectors, due to low responsivity and power dissipation. (b and c) Adapted with permission from Wiley.[72] (d) A PTE schematic mechanism when the light shines on one side of the material, a localized heating temperature difference (ΔT) is established, which causes a voltage difference across the channel that is proportional to ΔT and the Seebeck coefficient of the material. (e) The relationship between S of a material and its chemical potential with the energy band diagram of different types of junctions and the position of the Fermi level, adapted with permission from Wiley.[79]

converts it into heat, and it leads to a localized temperature increase. The temperature gradient creates a concentration difference for mobile charge carriers, which are either holes or electrons within the material. The region exposed to light has a higher concentration of these mobile carriers compared to colder regions in order to reach equilibrium. This diffusion creates an electric field within the material, which ultimately results in a measurable voltage (ΔV) across the channel.[75,76]

Predicting the photocurrent direction in PTE detectors is more complex due to the non-monotonic relationship between the Seebeck coefficient (S) and the chemical potential of the material, which does not follow a simple linear relationship. This non-monotonic behavior makes it challenging to predict the direction of the Seebeck effect-driven current. Fig. 4(e) shows the direction of the current with p–n and p–p junctions with weakly (p–) and heavily (p+) doped configurations.[77,78]

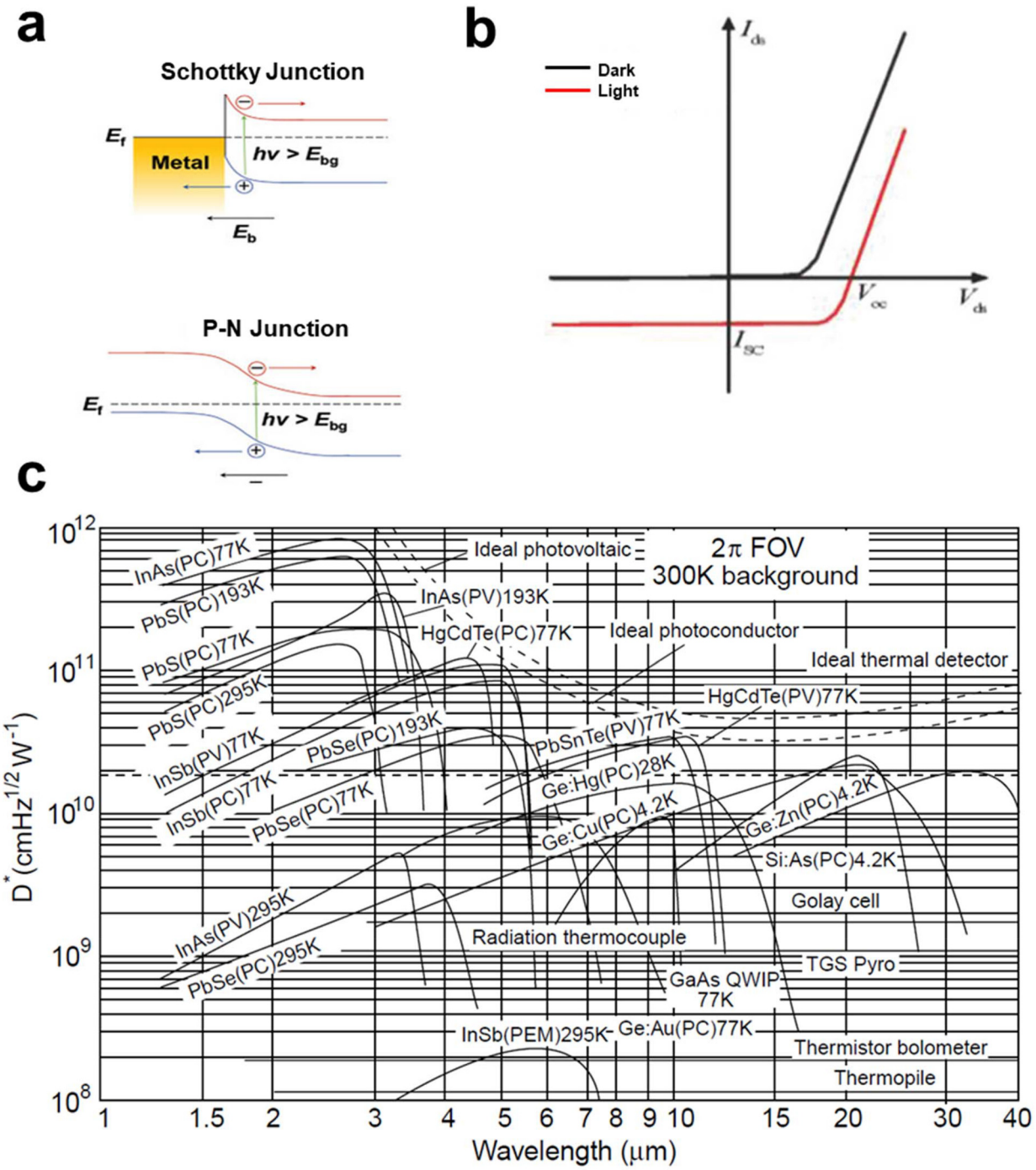

Fig. 5 (a) Schematic representation of the PVE mechanism that is commonly used in two types of junction and a Schottky junction, which is formed between a metal and a semiconductor, and the work function difference between them in order to create a depletion region and a built-in electric field, in the P–N junction, which is formed between two different doped regions of the same semiconductor material and doping introduces impurities that alter the conductivity, adapted with permission from Wiley.[71] (b) I–V curves showing the relationship between the current (I) flowing through a device and the applied voltage (V), adapted with permission from Wiley.[72] (c) Detectivity* of various commercially available IR detectors that operate at different temperatures with respect to wavelength, adapted with permission from Elsevier.[52]

Table 2 Comparison of photodetectors with different mechanisms and noise types

Features	PTE detector	PV detector	PE detector	Bolometer	Ref.
Mechanism	Seebeck effect	e–h pair	Pyroelectric effect	Resistance changes with ΔT	79
Spectral range	Broadband	Narrowband	Broadband	Broadband	
Response	Slow	Fast	Slow	Slow	
Power source	Not required	Not required	Not required	Required	
Noise type	Johnson	Johnson	Dielectric loss, Johnson	Johnson	
Temp. stabilizer	Not required	Not required	Required	Not required	

4.5 Photovoltaic effect (PVE)

Light absorption within a material generates electron–hole pairs through the photovoltaic effect. These pairs consist of an excited electron that has gained energy and a hole. An internal electric field, which typically arises from the Schottky junction or a p–n junction, separates these electron–hole pairs, which is crucial for generating an electrical current. It creates a built-in electric field across the junction when two different types of semiconductor materials are joined. An electric field forces the generation of electron–hole pairs by pushing electrons in one direction and holes in the opposite direction, as shown in Fig. 5(a). Photodetectors that use the photovoltaic effect for light detection are known as photodiodes. This effect can be effectively achieved in many 2D materials *via* engineered techniques, such as horizontal or vertical stacking heterojunctions. These junctions are formed by stacking n- and p-type 2D semiconductors or by combining them with metals. A defining characteristic of photodiodes is their rectifying current–voltage (I–V) behavior. This behavior represents a small and nearly bias-independent forward and reverse current that exhibits an exponential rise with an increasing bias voltage, as shown in Fig. 5(b). The built-in electric field that is responsible for this behavior in 2D materials can be established *via* various approaches, such as heterojunction formation, which is where we combine n- and p-type 2D materials to create the built-in electric field at the interface. By introducing chemical doping, the dopant atom helps to change the conductivity of the material and influence the electric field. With the help of split-gate tuning, when we apply the split-gate electrode placed near the 2D materials, the carrier concentration changes, which in turn modulates the electric field. The contact metals with different work functions, which represent the energy required to remove an electron from a material, play a role in establishing the built-in electric field when different metals are used as contacts. The photocurrent flow direction in a photodiode is solely determined by the built-in electric field direction. The absorbed photons excite the e–h pairs when a device is exposed to light of sufficient energy. The built-in electric field then separates these pairs, which drives the electrons toward one electrode and the holes toward the other. This separation helps with regard to understanding the two key current types in a photodiode, such as the short-circuit current. This is where the separated electron–hole pairs generate a current that flows through the device, which is called a short-circuit current. Electron–hole pairs accumulate at opposite terminals, creating a potential difference known as the open-circuit voltage. A comparison of the detectivity of different photodetectors that are available commercially with operational temperatures of different ranges is shown in Fig. 5(c).

Table 2 shows a comparison of different types of photodetectors with the mechanisms, responses, and noise types that are present.

5. Fundamentals of 2D materials

Research on 2D materials has exploded in recent years; this is driven by their potential to revolutionize electronics and optoelectronics, along with their strong sensing ability.[80–82] These ultrathin materials offer exciting possibilities for flexible displays, high-performance energy storage devices, and advanced photodetectors. The last decade has seen a significant amount of interest in 2D materials due to exciting possibilities for future electronics and optoelectronics devices. These atomically thin materials hold potential for applications such as flexible displays, efficient energy storage, and next-generation photodetectors.[83] Their unique property of having a band gap that changes with thickness opens doors for innovative device designs. Graphene is a frontrunner, but other exciting materials, such as black phosphorus (BP), indium selenide (InSe) and TMDCs, are emerging as promising 2D materials that can be easily exfoliated into atomically thin layers due to weak interlayer forces, which make exfoliation techniques such as chemical and mechanical methods highly effective. 2D materials promise to revolutionize various aspects of electronics with their diverse characteristics.

5.1 Black phosphorus (BP)

Black phosphorus (BP) exhibits a fascinating property known as a thickness-dependent bandgap. BP possesses a direct bandgap that is approximately 1.5 electron volts (eV) in its monolayer form. This value signifies the minimum energy that is required to excite an electron from the valence to the conduction band in a monolayer of BP. The bandgap reduces to 0.3 eV as the number of layers increases.[84,85] This unique characteristic enables precise control over the electrical conductivity of BP based on its thickness.[86,87] This unique property makes it useful for the near-infrared and mid-infrared range of the electromagnetic spectrum. This spectral range is crucial for various applications, such as night vision and thermal imaging. BP also boasts high carrier mobility and electrons can easily move through the material. This characteristic

is essential for efficient optoelectronic devices. Furthermore, BP demonstrates compatibility with a wide variety of substrates, which simplifies device fabrication processes. BP's high carrier mobility, moderate bandgap, and broad substrate compatibility make it, in essence, a strong contender for next-generation broadband optoelectronic devices.[88,89] The main characteristic of black phosphorus lies in its layered structure. Strong covalent bonds connect the phosphorus atoms within each layer, which form a highly stable network. However, weaker van der Waals interactions hold them together between these individual layers. This disparity in bonding strength allows for the potential exfoliation of black phosphorus into atomically thin sheets. Furthermore, the arrangement of atoms in bulk black phosphorus follows an orthorhombic crystal system, and it specifically belongs to the space group *C*-centered monoclinic, centered on the *a*-axis, and centered on the *c*-axis (*Cmca*), as shown in Fig. 6(a and b). This crystal structure creates the unique physical and electronic properties of black phosphorus, which include its anisotropic behavior (varying depending on direction) and its potential applications in next-generation IR detectors.[90,91]

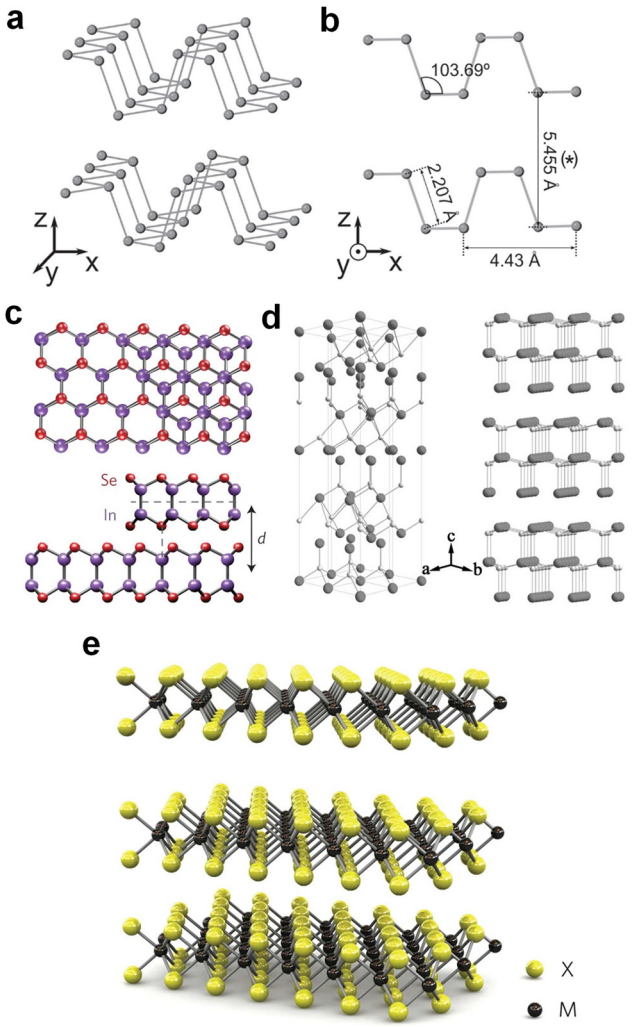

Fig. 6 (a) Crystal structure of BP, which is obtained *via* theoretical calculations using density functional theory (DFT), exhibits a puckered honeycomb lattice and weak interlayer forces. (b) Side view. (a and b) Adapted with permission from IOP.[104] (c) Crystal structures of two indium selenide (InSe) variations, which include the monolayer and bilayer, and the purple and red spheres represent individual atoms within the structure for indium (In) and selenide (Se), adapted with permission from Nature Springer.[105] (d) Crystal structures of two α-In_2Se_3 polymorphs, namely, α(3*R*)-In_2Se_3 and α(2*H*)-In_2Se_3. They consist of layers made from Se–In–Se–In–Se units. The indium (In) and selenium (Se) atoms are covalently bonded within a layer for strong intralayer bonding, adapted with permission from Wiley.[106] (e) 3D schematic representation of the layered crystal structure of MX_2, adapted with permission from Nature Springer.[107]

5.2 Indium selenide (InSe)

InSe has emerged as a promising material for nanoelectronics and optoelectronic applications. InSe has a high carrier mobility, which enables electrons to travel efficiently with minimal resistance and helps with regard to faster signal processing and better device performance.[92,93] It has a small effective electron mass. Electrons have a constant mass, so how they move within a material can be influenced by the material's structure. A small effective mass in InSe signifies that electrons behave almost like they are free and unhindered; this leads to faster movement and improved device performance. InSe exhibits broadband optical absorption that can effectively capture light across a wide range of wavelengths. This property is crucial for optoelectronic devices in the infrared range where light interacts with matter to generate a desired outcome, such as light detection or light emission.[94,95]

It falls under the category of layered metal chalcogenide semiconductors that have a unique structural arrangement. InSe consists of individual layers stacked upon each other. The honeycomb lattice structure of each layer is shown in Fig. 6(c and d). These planes consist of selenium (Se) atoms covalently bonded to indium (In) atoms, which are followed by another indium atom and then another selenium atom, to complete the honeycomb unit. Strong covalent bonds hold atoms together in specific planes within each layer of InSe. This unique atomic arrangement plays a significant role in the material's properties. InSe-based photodetectors and their heterojunctions have gained significant importance due to their impressive performance. These devices exhibit a broad range of light sensitivity, from wavelengths of 400 to 1000 nm.[96,97] InSe photodetectors also boast high photoresponsivity, which essentially signifies their efficiency in converting light into electrical current. This rapid response allows them to very quickly detect and react to changes in light intensity.[98,99]

5.3 Layered TMDC semiconductor materials

TMDCs stand out from other layered materials, such as graphene and boron nitride (BN), due to their unique optoelectronic properties. TMDCs offer a much wider range of possibilities, unlike graphene, because graphene is considered semi-metallic and has good conduction due to its Fermi level approximation to the conduction band with an almost zero bandgap and boron nitride, which acts as an insulator and

Table 3 2D material bandgaps: promising candidates for IR detection [E_g < 1 eV]

	Te		S		Se		
Bandgap (eV)	Monolayer	Bulk	Monolayer	Bulk	Monolayer	Bulk	Ref.
Pt	0.79	0.8	1.6	0.25	1.2	0.1	108–119
W	1.03	—	1.8–2.1	1.0–1.3	1.5–1.7	1.2–1.5	
Ti	—	—	0.02	—	—	—	
Zr	—	—	1.1–1.2	1.6	0.45	0.8	
Pd	0.3	0.2	1.1	—	1.3	0–0.1	
Ni	—	—	0.6	0.3	0.12	—	
Re	—	—	1.4	1.3	1.3	1.1	
In	—	—	—	2	2.5	1.26–1.3	
Sn	—	0.1–0.2	—	2.4	–	1.6	
Ge	—	—	3.4	1.5–1.6	2.2	1.08	
Mo	1.1–1.3	1.0–1.2	1.8–2.1	1.0–1.3	1.5–1.6	1.1	
Ga	—	1.7	2.6–3.1	1.61	2.1–2.2	2.0–2.11	
Nb	—	—	—	—	—	—	
Hf	—	—	1.27	1.6	0.61	0.6	
V	—	—	1.1	—	—	—	

does not conduct due to a large bandgap.[100] The key advantage of TMDCs lies in their tunable electronic properties, depending on the specific composition of the TMDCs, which involve transition metal and chalcogen atoms, so the material can exhibit a variety of bandgaps. The bandgap shows the difference in energy between the valence and conduction bands. This tunability of the bandgap in TMDCs allows them to range from semiconducting behavior, with a large bandgap and resistance to the easy flow of electrons, to metallic behavior, where the bandgap is very small. This versatility makes TMDCs highly attractive for various applications in electronics and optoelectronics, which is where precise control over electrical conductivity is crucial.

TMDCs are a class of layered materials with a unique crystal structure. They can be represented by the general formula MX_2, where M represents a transition metal atom and X represents a chalcogen atom, as shown in Fig. 6(e). It features a sandwich-like configuration, with a single layer of transition metal atoms positioned between two layers of chalcogen atoms.[101,102] Table 3 shows the bandgaps of 2D materials that are promising candidates for IR detection. One of the most captivating properties of TMDCs is their tunable electronic behavior. The bandgap, which signifies the difference in energy between an electron in its resting state and that at an excited state, can be manipulated by varying the specific combination of transition metal and chalcogen atoms within the MX_2 formula. This ability to control the bandgap is crucial with regard to optoelectronic applications. A direct bandgap is preferred for efficient light emission and absorption, whereas an indirect bandgap presents less favorable properties in this regard.[103]

The layered nature of TMDs unlocks exciting possibilities for tailoring their light–matter interactions. Precisely controlling the number of layers and the specific combination of elements paves the way for advanced optoelectronic devices with optimized performance. Their unique properties hold potential beyond optoelectronics for applications in quantum technologies and catalysis; this highlights their potential to revolutionize the field, and continuous efforts are aimed at harnessing the properties of TMDCs and enabling the development of groundbreaking devices with unparalleled functionalities and performance.

6. Key performance metrics for photodetectors

Photodetectors vary in shape and size, and they operate under different conditions. Evaluating their performance for specific applications involves considering a set of key parameters. These parameters provide a standardized way to compare how well different detectors convert photons into an electric current. Here are some of the parameters.

6.1 Detector signal and radiation power

The output of a detector signal, which is usually as a voltage or current, is a representation of incident radiation. This signal arises from the interaction between the radiation properties and the detector's internal mechanisms. The strength and characteristics of this signal depend on several important parameters, such as the detector bias voltage (V_b) that establishes the detector's operating point, which influences its sensitivity and responsiveness to incoming radiation. Modulation frequency (f) carries information by modulating a specific property, and this modulation frequency can be extracted from the detector output signal. Wavelengths (λ) of radiation interact with the detector material in various ways. The detector material's properties determine its absorption efficiency for different wavelengths, which directly affects the signal strength. The radiant flux (Φ) quantifies the amount of radiant power that shines on the detector's active area, and a higher radiant flux results in a stronger signal. The active area (A_{ds}) refers to the effective area of the detector that is exposed to radiation, and the operating temperature (T) of the detector material can influence its internal properties, such as carrier mobility and bandgap energy. These factors can impact the

detector sensitivity and potentially introduce noise into the output signal. It can be represented in the form of eqn (1) and (2):

$$V_s = V_b, f, \Phi, A_{ds}, T, \lambda \quad (1)$$

$$I_s = V_b, f, \Phi, A_{ds}, T, \lambda \quad (2)$$

6.2 Responsivity (R)

Responsivity measures the detector's ability to convert the incident light power into an electrical signal. It is measured as the ratio of change in photocurrent (ΔI) to the incident optical power (P) and the active area of a detector (A), as shown in eqn (3):

$$R = \frac{\Delta I}{PA} \quad (3)$$

It is expressed in A W^{-1} m^{-2}. A higher photoresponsivity represents a more efficient photodetector, which indicates that the device generates a larger electrical output for a given amount of incident light power.[120,121] There are two types of photoresponsivity, including current responsivity, which shows the generated photocurrent per unit of the incident light power, and it is commonly used for photoconductive and avalanche photodiode (APDs). Voltage responsivity relies on a built-in electric field within the material in order to separate light-induced electron–hole pairs, which give us voltage output, and it is represented in the photovoltage per unit of incident light power and is commonly used in photodiodes. Photovoltaic devices generate an open-circuit voltage under light irradiation due to the built-in electric field separating charges, and responsivity is shown by voltage responsivity. Most photodetectors have an external biasing for operation that is required to generate a photocurrent, and responsivity is shown as current responsivity. Photoresponsivity plays a vital role in selecting photodetectors for specific applications. A higher responsivity is generally desirable, especially for detecting weak light signals. However, other factors, such as noise level and spectral response also need to be considered for optimal detector selection.

6.3 Specific detectivity (D^*)

Detectivity (D^*) measures the detector's sensitivity and its ability to detect weak signals relative to its noise level. Imagine a photodetector that operates in a faded light environment. A sensitive detector would be able to distinguish the faint light signal from electrical noise within the device itself. A higher D^* indicates a more sensitive detector that can effectively separate the weak incoming light signal from background noise. There are two main categories of noise to consider, namely, radiation noise and intrinsic noise. Radiation noise originates from the random fluctuations of light itself, which will hinder a detector's ability to accurately sense light, and it is further classified as signal fluctuation noise that arises from the inherent statistical nature of light detection. Even a constant light source exhibits variations in the number of photons that arrive at the detector at any given moment, and background fluctuation noise arises from external sources of light, such as thermal radiation from the environment. Intrinsic noise originates within the photodetector itself, and it is not directly related to the incoming light. Shot noise is a common form of intrinsic noise in photodiodes. It arises from random fluctuations in the flow of electrical current within the device.[38] Background fluctuation noise is typically more significant in infrared detectors compared to signal fluctuation noise due to the nature of infrared radiation. Detectivity is expressed as a function of responsivity and expressed in Jones (J), as illustrated by eqn (4):

$$D^* = R\sqrt{\frac{A}{2eI_{dark}}} \quad (4)$$

A is the active area of the channel, R represents the responsivity, e denotes the charge on the electron (1.602×10^{-19} C), and I_{dark} is the dark current.

Cutting-edge photodetectors achieve an impressive specific detectivity (D^*) of 10^{12} Jones in the short-wave infrared (SWIR) region.[122] However, this performance degrades significantly at MWIR and LWIR wavelengths. This limitation arises from the dominance of the background-limited operation in these bands.

6.4 Photoconductive gain (G)

The photoconductive gain is a valuable property of photodetectors that enhances their sensitivity to weak light. It quantifies the ability of a detector to generate multiple electrical carriers for each absorbed photon. This amplification mechanism significantly improves the SNR, which allows for the detection of faint light signals.[72,123] The key factors that influence the photoconductive gain are the carrier lifetime and transit time. The carrier lifetime refers to the average time an electron or hole exists before recombining with an oppositely charged carrier. On the other hand, the transit time represents the time that it takes for a generated carrier to drift across the active region of the detector under an applied electric field. High gain is achieved when the carrier lifetime is significantly larger than the transit time.

$$\text{High gain} = \text{Carrier lifetime} \gg \text{Carrier transit time}$$

This enables a single photogenerated carrier to repeatedly traverse the channel, generating additional carriers through impact ionization. These secondary carriers further contribute to the current, resulting in a net amplification of the initial photocurrent. By amplifying the weak photocurrent, the photoconductive gain enables the detection of low-light signals. This is particularly advantageous in applications like night vision, medical imaging, and optical communication where sensitivity is essential. While photoconductive gain offers significant benefits, increased gain can lead to a higher dark current, a source of noise that can limit the overall detectivity of the detector. Additionally, achieving high gain often requires careful material selection and device design to optimize carrier lifetimes and transit times.

6.5 External quantum efficiency (EQE)

EQE is an important parameter that represents the efficiency of a photodetector in converting incident photons into usable electrical current. It essentially reflects the probability of an absorbed photon generating a charge carrier that contributes to the photocurrent. EQE is expressed as the ratio between the collected charge carriers and incident photons, as shown in eqn (5):

$$\mathrm{EQE} = \frac{\text{charge carriers}}{\text{incident photons}} = R\frac{hc}{e\lambda}(\%) \quad (5)$$

R (A W^{-1}) represents responsivity, c (m s^{-1}) is the speed of light in a vacuum (3.0×10^8 m s^{-1}), λ (nm) is the wavelength of incident light, e (C) is the elementary charge of an electron (1.602×10^{-19} C), and h (J s) is Planck's constant (6.634×10^{-34} J s).

When photons with energies exceeding the bandgap energy of the photodetector material are absorbed, electrons absorb the energy and jump to excited states that create holes behind them. To maximize the photocurrent, it is crucial that these generated carriers are collected by the electrodes before they recombine with oppositely charged carriers. Multiple factors influence the photodetector EQE, including the absorption coefficient, which shows the material's ability to absorb light of a specific wavelength. Charge collection efficiency reflects the effectiveness of collecting generated carriers before recombination, and internal quantum efficiency (IQE) indicates the ability to convert absorbed photons into free charge carriers that contribute to the photocurrent. By carefully selecting materials, designing device structures, and optimizing fabrication processes, we can maximize the EQE of photodetectors for specific applications.[124,125]

6.6 Shot and thermal noise

Shot noise is an inherent limitation of photodiodes, arising from the statistical nature of both the dark current and the photocurrent. When photodiodes operate in photoconductive mode, *i.e.*, with an applied bias voltage, the shot noise becomes the dominant source of noise. This noise originates from random fluctuations in the arrival times and number of individual charge carriers generated within the detector. The magnitude of shot noise can be quantified by its root mean square (RMS) value, which represents the standard deviation of the current fluctuations and shown in eqn (6):

$$I_{\mathrm{shot}} = \sqrt{2q\left(I_{\mathrm{Photo}} + I_{\mathrm{dark}}\right)\Delta f} \quad (6)$$

where q is the charge on an electron (1.6×10^{-19} C), and Δf is the frequency bandwidth of the system and the standard unit for the shot noise current is Ampere (A).

Thermal noise, also called Johnson noise, arises from the random motion of charge carriers within the photodetector's resistive elements. This phenomenon is due to inherent thermal energy present in any material at a non-zero temperature. As the temperature increases, the thermal energy produces charge carriers with greater kinetic energy, causing them to vibrate more intensely. These random vibrations lead to fluctuations in the current flow and are expressed in eqn (7):

$$I_{\mathrm{thermal}} = \sqrt{\frac{4kT\Delta f}{R}} \quad (7)$$

where k is Boltzmann's constant (1.380×10^{-23} J K^{-1}), T is the temperature, and R is the resistance, and I_{thermal} has the unit of Ampere (A).

6.7 Noise equivalent power (NEP)

NEP is used to characterize the sensitivity of a photodetector by distinguishing the minimum amount of optical power incident on the detector and the inherent noise of the detector and its associated circuitry. A lower NEP value indicates greater sensitivity of the detector, which can efficiently detect weaker signals from the noise. It can also be related to a detector's responsivity (R), which represents the ratio of its output signal (current or voltage) to the incident optical power. The relationship can be expressed as eqn (8):

$$\mathrm{NEP} = \frac{I_{\mathrm{n}}}{R} \quad (8)$$

R represents the responsivity, I_{n} shows the noise current, and NEP is expressed in watts.

The above equation highlights the inverse relationship between NEP and responsivity. A detector with higher responsivity will have a lower NEP, indicating better sensitivity for detecting weak signals. Due to their thin nature, 2D materials inherently possess a limited carrier transport volume. This restricted volume translates into a higher intrinsic resistance within the material. Consequently, for IR photodetectors fabricated using 2D materials, the inherently lower current can lead to reduced noise levels compared to bulk semiconductor-based devices.[126,127]

7. 2D material-based IR photodetectors

The initial development of 2D material-based infrared detection favored the photoconductor configuration due to its inherent gain mechanism and simple fabrication process. This configuration typically involves a basic structure with contacts, a layer of 2D material for light absorption, and a back-gate electrode used for electrostatic control over the conductivity of the 2D material channel on the insulating gate substrate. Table 4 summarizes the key performance parameters of various 2D material-based IR photodetectors. In this section, we highlight recent advancements in IR photodetectors utilizing various 2D materials as light absorbers and the progress achieved with different categories of 2D materials.

7.1 Widely tunable IR photodetector based on vdWHs

2D materials, forming vdW heterojunctions, offer exciting possibilities for high-performance infrared (IR) photodiodes. These structures are promising due to tailored bandgap align-

Table 4 Essential performance metrics of broadband photodetectors utilizing 2D materials

Material	Wavelength	R [A W^{-1}]	EQE [%]	Rise, fall time	Ref.
Gr–$MoTe_2$–hBN–Gr	800–1100 nm	88		330 μs	139
Gr–Bi_2Te_3	532–1550 nm	35	83		140
Gr–Si waveguide	2.75 μm	0.13			121
WS_2	460–647 nm	9×10^{-5}		5.3 ms	141
n-Doped Gr QD	310–1000 nm	324 V W^{-1}		50 s, 10 s	142
WS_2–Gr	340–680 nm	950		7.85 s, 5.61 s	143
Graphene	1 mm	0.07–0.15 V W^{-1}			144
Monolayer graphene	532 nm–10 μm	8.61–0.4		30 s	145
Gr–Ta_2O_5–Gr	532 nm–3.2 μm	1000–1.1			120
BP carbide	2.004 μm	2163	10^4	0.7 ns	146
GaTe	254–710 nm	274.3			147
PbS–Gr	410–750 nm	2.8×10^3		1 s, 10 s	148
WSe_2–SnS_2	400–900 nm	244		13–24 ms	149
PPh_3–ReS_2	520–1064 nm	10^6		30–64 ms	150
GO–Gr nanoribbons	1550 nm	1	80	2 s, 29 s	151
MoS_2–$MoTe_2$	560–1550 nm	0.046		25–60 μs	152
Graphene	457–785 nm	4×10^{-3}			153
EO–EGr	350–470 nm	200			154
InSe–Gr	400–1000 nm	60–5.3		120–100 μs	155
BP	532 nm–3.39 μm	1000–82	10^4	0.13 ms	156
BP	3.7–7.7 μm	0.518–0.0022			157
Gr–hBN–MoS_2	400–885 nm	180		0.23–0.25 s	158
ReS_2	450–800 nm	3000			159
Graphene	30–220 μm	10^{-8}		10 ps, 50 ps	160
ZnO–Gr	325–445 nm	10^4	10^7		161
MoS_2	450–633 nm	0.05–0.12			162
BP	640–940 nm	4.8×10^{-3}		1–4 ms	86
Gr–MoS_2–Gr	458–633 nm	0.068	65		163
GaSe	254–700 nm	2.8	1367	20 ms	164
SnTe	405 nm–3.8 μm	3.75		0.31 s, 0.85 s	165
BP/AsP	1–4.6 μm	17		8.6–12.4 μs	166
Graphene	1550 nm	0.5×10^{-3}	16		167
BP	315–1240 nm	9×10^4	10^8	1 ms, 4 ms	168
Gr/y/Gr	300–1100 nm	1			169
Plasmon–graphene	450–650 nm	6.1×10^{-3}	1500		170
Gr–$MoSe_2$–Gr	473–1064 nm	0.11	12.9	24 μs	171
GNR	10.6 μm	8×10^{-6}			172
$MoTe_2$–$PdSe_2$	2000 nm	1.2×10^5	48	2 ms	11
p-BP–n-$PdSe_2$	1064, 1310 nm	4.5×10^5	10^6		173
BP–WS_2	600 nm	0.5	103		12
Bi_2Te_3–Si	370 nm–118 μm	1		100 ms	174
MoS_2	380–700 nm	0.57		70–110 μs	175
SnS_2	300–800 nm	2.06×10^{-4}			176
BP	400–1700 nm	4.5×10^{-4}			177
WSe_2–MoS_2	514–633 nm	0.05	12		178

ments, enhanced carrier transport, and strong light absorption. Black phosphorus (BP) has emerged as a promising material for mid-infrared detection devices due to its tunable bandgap for absorbing light in the mid-infrared range, high carrier mobility, and intrinsic layer structure.[128,129] Chen *et al.* presented the influence of a vertical electric field on the light detection range of a 5 nm thick BP detector.[46] Because of the Stark effect, the electric field dynamically extends the photoresponse from 3.7 μm to 7.7 μm. The device exhibited a peak extrinsic photoresponsivity of 518 mA W^{-1} at 3.4 μm, decreasing to 30 mA W^{-1} and 2.2 mA W^{-1} at 5 μm and 7.7 μm, respectively. Moreover, the analysis of photocarrier lifetime, which represents the average time for the excited electron to exist before recombination, suggests the potential for high-speed operation at 1.3 GHz. A new mid-IR photodetector design uses black phosphorus sandwiched between h-BN layers. This "hBN–BP–hBN" structure creates a clean interface for efficient light capture and protects the BP from oxidation, as shown in Fig. 7(a). The device fabrication process involves a polymer-free dry transfer technique for the BP/h-BN assembly onto a SiO_2 substrate. This substrate is equipped with a 90 nm thick layer of silicon dioxide (SiO_2) for optimized electrical performance and surface passivation. An optical image of the devices is shown in Fig. 7(b). Later on, Huang *et al.* demonstrated the integration of BP photodetectors with silicon-on-insulator (SOI) waveguides.[130] Achieving seamless integration between waveguides and on-chip sensing systems remains a significant hurdle, despite ongoing research due to lattice mismatch, which refers to the disparity in atomic spacing between different materials. When this mismatch is substantial, it leads to the formation of defects and strain at the interface where the materials meet. These defects and strains ultimately degrade the overall performance of the sensing system. The high carrier mobility of BP, often exceeding 1000 cm^2 V^{-1} s^{-1}

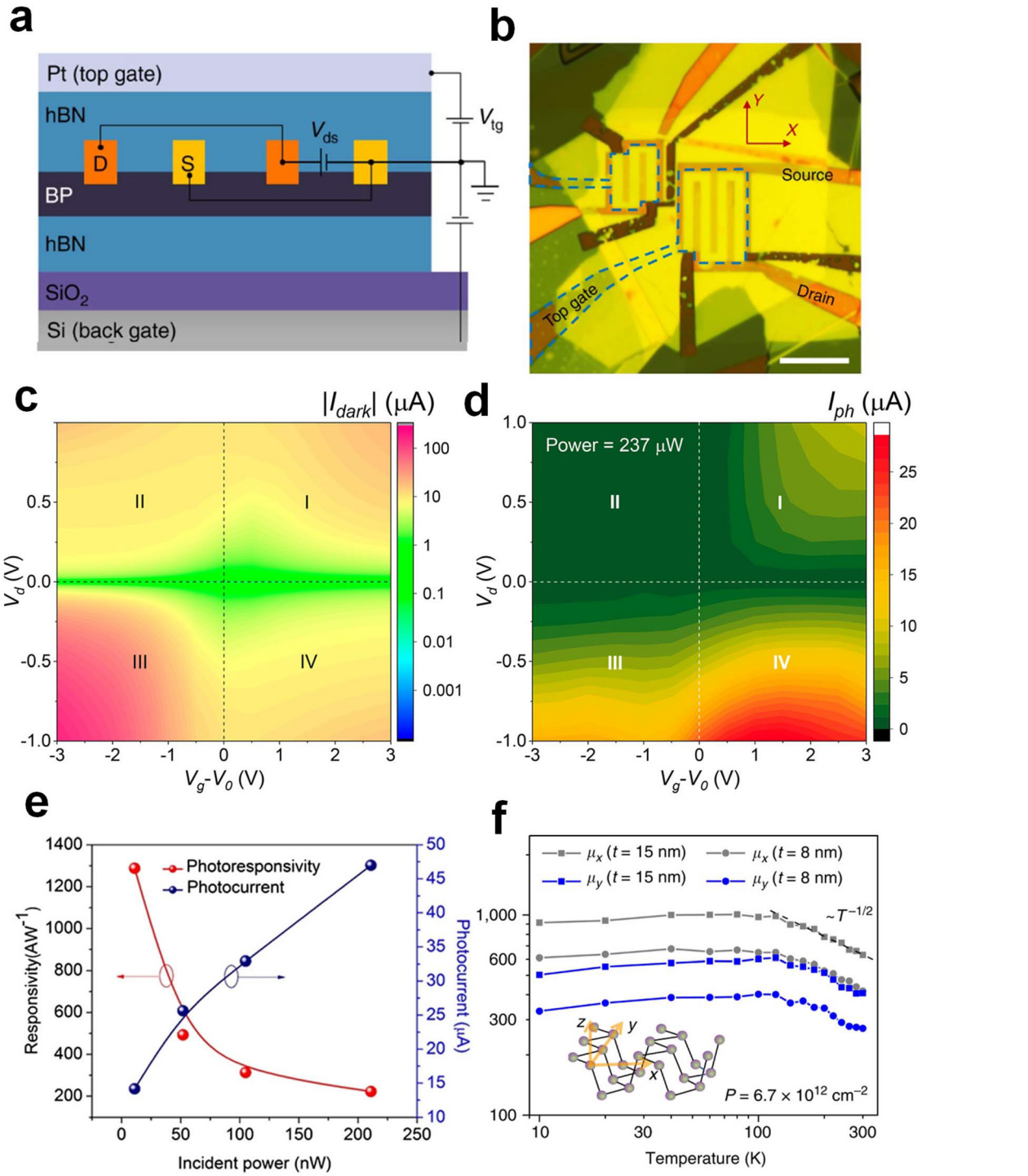

Fig. 7 Widely tunable IR photodetectors. (a and b) Schematic and optical image of a mid-infrared (mid-IR) photodetector utilizing BP in a dual-gate transistor, which enables enhanced control of the electric field from both sides of the BP channel, offering greater tunability. hBN serves as the gate dielectric both on top of and at the bottom of the device, providing electrical insulation between the gates and channel. BP acts as an active channel material responsible for light absorption and photocurrent generation, adapted with permission from Nature Springer.[46] (c and d) Electrical properties of a widely tunable BP mid-infrared detector as a function of gate bias that controls the electric field across the BP channel, influencing the conductivity and drain bias, which in turn influence the flow of current between the drain and source terminals. The device shows an optimal photocurrent at the negative drain bias, which helps to reduce the barrier for hole transport and capture photogenerated electrons that contribute to photoconductive gain and amplify the overall current, adapted with permission of ACS.[130] (e) High photocurrent and responsivity of 1.3 × 10^3 A W^{-1} at 1550 nm with encapsulation of graphene, to protect BP from environmental degradation, which ensures the long term stability and performance of the device, adapted with permission from ACS.[133] (f) Hall effect mobility measured along two in-plane directions, *x* and *y*, shows that thicker films consistently exhibit higher mobility than thinner films because thicker films potentially offer a more complete and defect-free channel for charge carriers to travel through, leading to higher mobility, adapted with permission of Nature Springer.[138]

at room temperature, plays an important role in enhancing responsivity and gain.[131] Upon photoabsorption, e–h pairs are generated within the BP material. Due to the inherently high carrier mobility of BP, these photogenerated carriers are rapidly transported under an external electric field, resulting in reduced transit time and high photoconductive gain. This gain mechanism enables a single photogenerated carrier to contribute multiple times to the photocurrent before recombining, resulting in an amplified current response under a given optical input. Even in the absence of significant gain, high mobility ensures a greater proportion of photogenerated carriers are efficiently collected at the contacts before non-radiative recombination occurs, thereby maximizing the quantum efficiency and boosting the overall responsivity of the BP-based photodetector.[132] The device exhibits a significant drain current at negative values of both gate voltage (V_g) and drain voltage (V_d), as shown in Fig. 7(c). This behavior is characteristic of the "on-state" for a p-type dominant ambipolar transistor. In the electron-conducting regime, where V_g is greater than V_o, the drain current exhibits a slight increase compared to the off-current but remains lower than the on-current observed in the hole-conducting state. This behavior of the dark current is primarily influenced by the carrier type, concentration and barrier height. In the p-type dominant regime, a large number of holes readily flow, resulting in a high on-current. Conversely, applying a positive V_g favors the accumulation of electrons, forming a higher barrier for hole conduction and resulting in a low off-current. The intermediate electron-conducting regime exhibits a slightly higher current than the off-state due to the presence of some electrons, but it remains lower than the on-current due to the limited number of available electrons and the potential barrier hindering their flow and photocurrent, which depends on the gate and drain bias, as shown in Fig. 7(d). In another study, Li *et al.* reported a graphene–BP vdW heterostructure photodetector with high responsivity and long-term stability for IR detection.[133] The top layer of graphene acts as an encapsulation layer to protect the BP from environmental degradation while ensuring long-term stability and efficient transport of carriers. Under light conditions, the top graphene layer helps separate electron–hole pairs created within the BP layer and reduces the potential barrier between the BP and metal electrodes and achieves a high responsivity of 1.3×10^3 A W^{-1} at 1550 nm. This responsivity is 213 000 times that of monolayer graphene devices and 2000 times the pure BP phototransistor,[134,135] as shown in Fig. 7(e). The electrical properties of BP thin films were investigated using the angle-resolved Hall mobility technique, which measures how easily charge carriers move within the material in different directions (X or Y) at various temperatures. BP films exhibit anisotropic behavior that conducts better along the X-axis than the Y-axis. The mobility along the X-axis was about 1.8 times higher than that along the Y-axis, as shown in Fig. 7(f). Additionally, thicker BP films showed higher overall mobility compared to thinner films, suggesting the influence of the underlying substrate on carrier movement.[136,137]

7.2 Next-generation IR photodetection from 2D/3D vdWHs

The emergence of 2D materials offers exciting possibilities for a new generation of infrared detectors, which play a vital role in various defense, military, and astronomy applications. However, limitations like restricted thickness and fabrication techniques have hindered their full potential, resulting in a low light detection efficiency and slow response times. 2D/3D hybrid vdW heterostructures for infrared detection combine the distinctive properties of 2D materials with the advantages of established 3D materials. This hybridization offers significant potential to address the limitations of individual materials and pave the way for high performance, next-generation infrared detectors.

A comparison of the bandgaps of 2D and 3D materials, along with their spectral responses, ability to detect light of various wavelengths, and the light source used for measurements is shown in Fig. 8(a). In the figure, hollow symbols represent the measured results obtained using a laser source. Lasers typically emit light within a highly specific and narrow wavelength range, allowing for precise measurement of the material response at that specific wavelength. Solid symbols and lines represent the results measured using a blackbody source. Blackbody sources emit light across a broad spectrum of wavelengths, providing information on the material's response to a wider range of illumination. Many 2D layered materials exhibit a superior photoelectric conversion efficiency (PCE) compared to traditional thin films; this shows the potentially higher intrinsic ability of 2D materials to generate a photocurrent due to their high efficiency at absorbing light because of their unique atomic structure, direct bandgap and reduced recombination. A comparison of 2D materials and conventional thin films is shown in Fig. 8(b). In another study, Gao *et al.* reported the observation of ballistic avalanche effects in InSe/BP heterostructures for mid-infrared light detection. Carrier multiplication, which is crucial for single-photon detectors and transistors, is explored through the sub-mean-free-path (MFP) in vertically stacked InSe/BP heterostructures that facilitate the development of APDs capable of detecting MIR light at a wavelength of 4 μm, along with impact ionization transistors featuring an exceptionally steep subthreshold swing (below 0.25 mV dec^{-1}), which highlights the potential of sub-MFP InSe/BP heterostructures for designing next-generation devices with improved performance due to their efficient carrier multiplication capabilities.[179] Light-detection elements with high efficiency are crucial for mid-infrared light detection and ranging (LIDAR), quantum information processing and single-photon detection applications.[180,181] APDs are particularly promising because they amplify the signal using an external electric field, resulting in high sensitivity. I–V characteristics of APDs under dark and light conditions at low temperatures are shown in Fig. 8(c). The current flowing between the drain and source exhibits a high multiplication factor of up to 3×10^4 at $V = -4.3$ V. A photocurrent generation mechanism in the BP/InSe photoconductive detector under different light illumination is shown in Fig. 8(d). This demon-

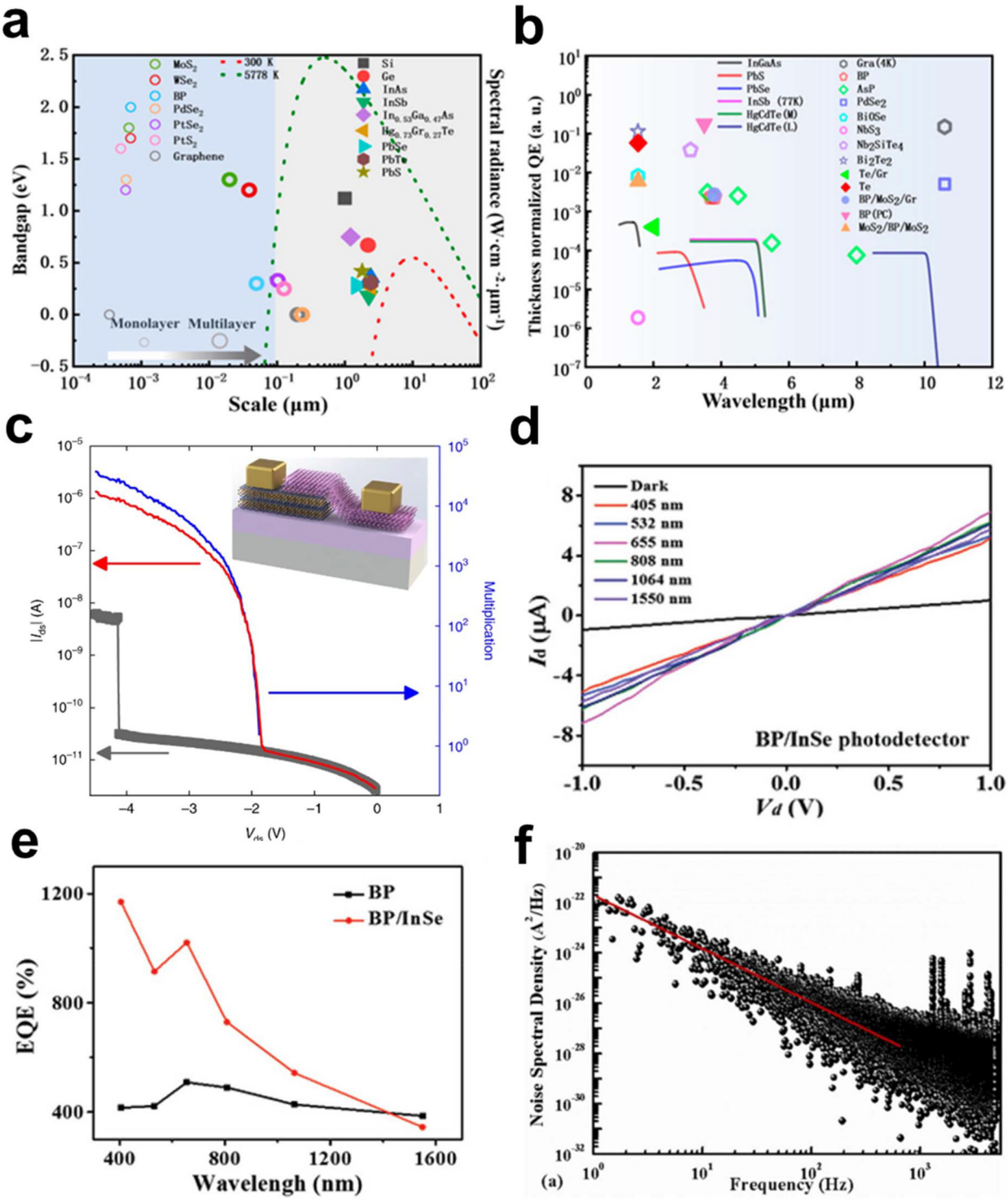

Fig. 8 Next generation IR detectors from 2D/3D vdWHs. (a) Comparison of bandgap differences and spectral radiance for 2D and 3D materials. (b) Thickness dependent normalized EQE of 2D layered materials and conventional thin films. (a and b) Adapted with permission from MDPI.[182] (c) *I*–*V* characteristics of InSe/BP APD at low temperature (10 K) represent the photocurrent and multiplication factor, an applied electric field causes an avalanche multiplication effect represented by a blue line. Electron–hole pairs are generated with the absorption of photons, a strong electric field accelerates these carriers and gives them enough energy to further ionize atoms within the material that in effect create additional electron–hole pairs leading to avalanche multiplication of the initial photocurrent. Inset shows the structure of InSe/BP APD, stacked to form a photodetection region, adapted with permission from Nature Springer.[179] (d) Photocurrent response of the BP/InSe based detector, showing the increase in photocurrent compared to that in the dark due to carrier screening and competing recombination pathways. (e) EQE of pristine BP and BP/InSe over the wavelength range of 405–1550 nm is represented by black and red curves, respectively. (d and e) Adapted with permission from Wiley.[183] (f) Noise performance of InSe/$ReSe_2$ vdWH shows the flicker noise dominating the low-frequency region, a lower NEP value signifies a more sensitive detector that can detect weaker signals from background noise, adapted with permission from Elsevier.[184]

Table 5 Fast photoresponse of infrared photodetectors based on 2D materials

Material	Wavelength (nm)	Frequency (GHz)	Speed	Ref.
Gr	1550	40	0.36 ps	167
PbSe/TiO_2/Gr	350–1950	—	50–83 ns	185
BP carbide	2004	—	0.7 ns	146
Gr/Si	1550	41	50 Gbps	186
Graphene	1550	262	2.1 ps	187
Gr/$MoSe_2$/Si	365–1310	—	350 ns	188
Graphene	1550	16	10 Gbps	21
BP/Si	1550–1580	3	3 Gbps	189
Gr	800	500	4 ps	190
Ge/Si	1310	340	40 Gbps	191
Graphene	1450–1590	20	12 Gbps	192

strates the increase in the current intensity of the BP/InSe photodetector when illuminated with 655 nm light, compared to in darkness, which implies that the high photoresponsivity and dark current appear to be suppressed under illumination. The BP/InSe photodetector exhibits a significantly enhanced EQE in the broadband light spectrum. This exceptional light-to-current conversion efficiency, exceeding 100% for both BP and InSe devices, is attributed to an internal gain mechanism within the BP layer, as shown in Fig. 8(e). The BP/InSe photodetector exhibits an EQE ranging from 344% to 1170% across a wavelength spectrum of 405 nm to 1550 nm. The different heterostructures of BP and InSe have shown promising results for next-generation infrared photodetectors. In the InSe/$ReSe_2$ van der Waals (vdW) heterostructure, the measured noise current power spectral density exhibits typical 1/*f* noise behavior at low frequencies and refers to a type of electrical noise where the intensity increases with a decrease in frequency, as shown in Fig. 8(f). It represents the minimum light signal power required for the signal-to-noise ratio to reach 1, given in W $Hz^{-1/2}$. The fast photoresponses of IR detectors based on 2D materials with different operating wavelengths, frequencies, and speeds are shown in Table 5.

7.3 Ultrasensitive infrared (IR) photodetectors based on 2D/3D materials

2D semiconductors and their vdW heterostructures have become a promising platform for infrared (IR) photodetectors. These photodetectors can sense not only the intensity of light but also the direction of its electric field oscillation. This capability makes them valuable for various applications in optoelectronics and communication due to their potential for improved information density, reduced noise, and enhanced functionality in devices like optical modulators and high-speed data transmission systems.[193] In a recent study, Waqas *et al.* presented an ultrasensitive near-infrared photodetector based on the violet phosphorus (VP) and InSe van der Waals heterostructure. The type-II VP/InSe vdWH combination offers a unique configuration for efficient optoelectronic devices.[197] Under near-infrared light excitation at 1064 nm, the detector exhibits an impressive responsivity of 182.8 A W^{-1} and an impressive detectivity of 7.86×10^{12}. A schematic of the device structure is shown in Fig. 9(a). The violet phosphorus (VP) single crystal is fabricated using physical vapor transport, which creates thin films on a substrate surface.[194] Physical vapor transport is a vacuum-based process that relies on physically removing material from a source and then depositing it on the target substrate in a controlled manner. The device exhibits remarkable stability in its photocurrent response, which can detect extremely weak light signals with a power density as low as 0.021 mW cm^{-2}. Under 1064 nm wavelength illumination and a power density of 0.021 mW cm^{-2}, the detector achieves a maximum responsivity (R) of 182.8 A W^{-1} and a detectivity (D^*) of 7.86×10^{12} Jones, as shown in Fig. 9(b). In another study, Xiao *et al.* presented the RGO–MoS_2/pyramidal Si heterojunction, which offered ultrahigh detectivity and broadband photodetection capabilities. The photodetector's response to varying light wavelengths, ranging from 350 to 1050 nm, was measured, and peak sensitivity was observed between 800 nm to 900 nm, which showed the UV-vis-NIR absorption spectra of the materials. Due to the broad light absorption properties of the RGO–MoS_2 composite film, the device also demonstrates a significant photovoltaic response at longer wavelengths, specifically 1310 nm and 1550 nm, as shown in Fig. 9(c). In another study, Wu *et al.* showed a large-area photodetector based on a mixed-dimensional vdW heterojunction between 2D palladium diselenide ($PdSe_2$) and three-dimensional (3D) cadmium telluride (CdTe). By leveraging the broad light absorption of the multilayer $PdSe_2$, with a high-quality interface and mixed-dimensional design, the device achieves exceptional infrared light detection capabilities at room temperature. It can detect a remarkably wide range of light wavelengths, extending all the way to long-wave infrared (LWIR) at 10.6 μm. Furthermore, the photodetector demonstrates a good ability to track short infrared pulses with a fast response time of 70 ns. The *I–V* characteristics of the photodetector under light of various wavelengths, ranging from ultraviolet (UV) to mid-infrared (MIR), are shown in Fig. 9(d); these demonstrate the photodetector's broad spectral response, with sensitivity observed from 265 nm to 3043 nm.[195] In another study, Wang *et al.* reported a high-performance IR detector made from a graphene/hyper-doped silicon heterostructure. This design incorporated graphene as a carrier transport layer to improve the efficiency of separating and collecting charges within the device compared to a standard hyper-doped silicon photoconductor. The improved efficiency resulted in remarkable EQEs of 7.37% and 97.26% at 1550 and 1310 nm, respectively, at a low voltage of V = 0.3 V. The device without graphene shows an increase in external quantum efficiency (EQE) with higher bias voltage, reaching a maximum of 15.36% at 1310 nm under 3.0 V. In contrast, the graphene-based photodetector achieves a significantly higher EQE, exceeding 43% at 1310 nm with a much lower bias voltage of 0.1 V. The peak EQE surpasses 100%, indicating a strong photoresponse, as shown in Fig. 9(e). This remarkable improvement highlights the effectiveness of the graphene layer at enhancing carrier transport and boosting the overall photodetection performance. Even at longer wavelengths of

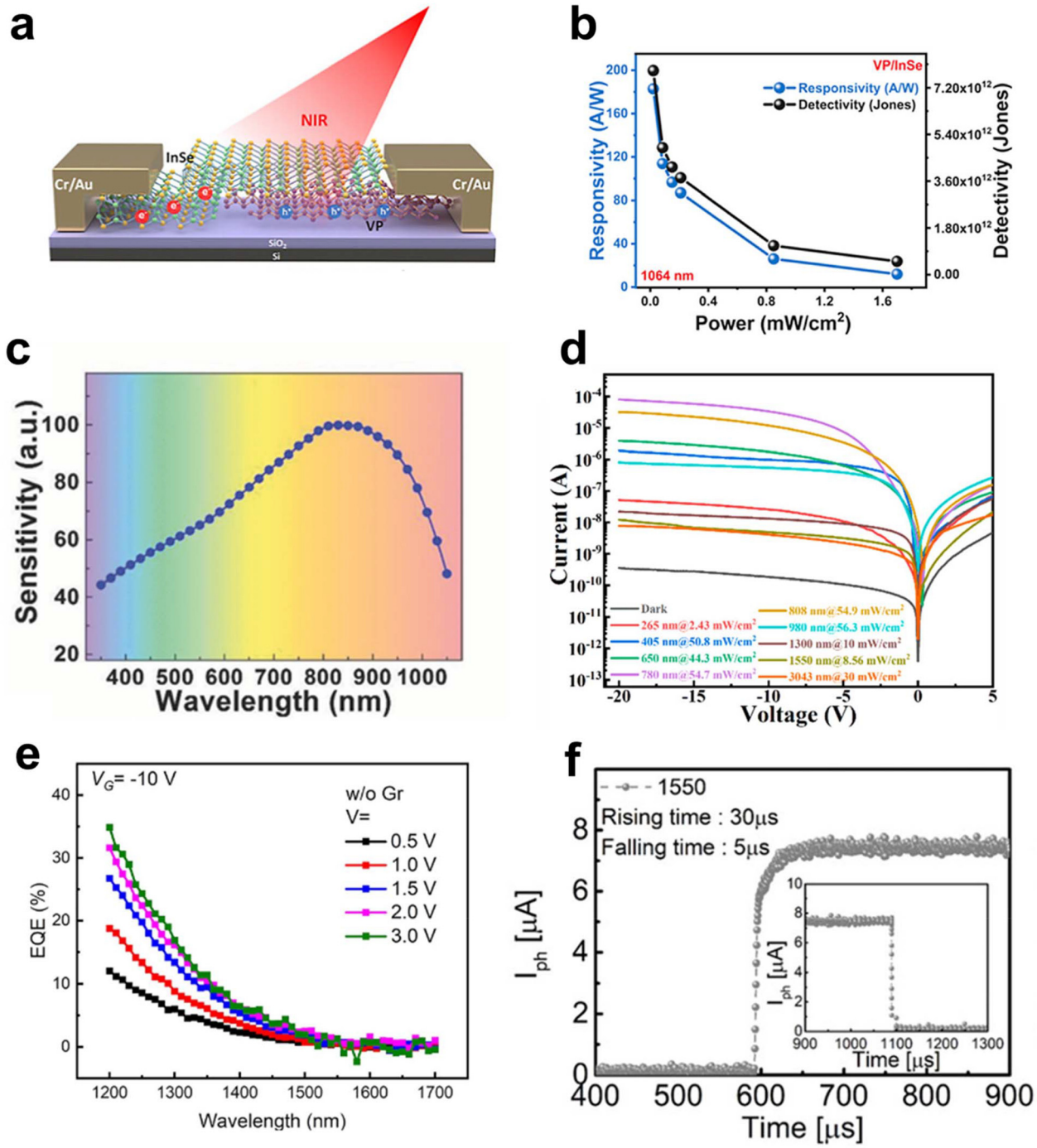

Fig. 9 Ultrasensitive IR photodetector. (a) Schematic diagram of type-II VP/InSe vdWHs (b) at 1064 nm and under an incident power density of 0.021 mW cm^{-2}, the device demonstrates a peak responsivity (R) of 182.8 A W^{-1} and D^* of 7.86 × 10^{12} J. (a and b) Adapted with permission from ACS Nano.[197] (c) Ultra-broadband detection and high responsivity measured across varying wavelengths ranging from 350 to 1100 nm, adapted with permission from Wiley.[198] (d) I–V characteristics of the $PdSe_2$/CdTe heterojunction device measured under various light wavelengths ranging from 265 to 3043 nm, adapted with permission from ACS Nano.[195] (e) Si : Ag detector without graphene demonstrates an EQE of 97.26% at 1310 nm and 7.37% at 1550 nm using a low bias voltage of V = 0.3 V, adapted with permission from Elsevier.[199] (f) Transient photoresponses of the p-WSe_2/n-Ge photodiode at a reverse bias of −1.5 V, showed rise and fall times of 30 and 5 μs at 1550 nm, respectively. Adapted with permission from Wiley.[196]

1550 nm, the device exhibits a high EQE of 7.37% under low voltage. In another study, Lee *et al.* demonstrated p-WSe_2/n-Ge heterojunctions for their potential as an ultra-high-speed, broadband photodetector. The performance of these devices was compared with different n-Ge regions fabricated using ion implantation. The photodetector fabricated with a standard, long, and lightly doped n-Ge region exhibited a broad spectral response, detecting light from the visible range to near-infra-

Table 6 High-speed infrared (IR) detection based on 2D materials

Material	Wavelength (μm)	R (A W^{-1})	D^* (Jones)	Rise/fall time	Ref.
MoS_2–Gr	0.4–2	376	10^{10}	0.6 s	200
BP-carbide	0.5–8	2163	10^{14}	0.7 ns	146
WS_2–Si	0.2–3	0.02	10^{13}	4.5/21 ms	201
$PdSe_2$	0.2–4.6	0.72	10^{14}	3.5/3.9 μs	202
BA-P	0.5–8.2	0.2–0.1	10^{9}	0.5 ms	203
$PtTe_2$–Si	0.2–10.6	5–0.67	10^{9}	2.4 μs	204
BP–InSe	0.45–1.55	43.11	—	22 ms	205
CoSe	0.45–10.6	2.58	10^{9}	73/80 ms	206
Graphene	300–30	30 V W^{-1}	10^{10}	0.9/1.4 ns	207
Tellurene	0.52–3.39	19.2 m	—	4.3 ns	208
BP	0.95	4.8 m	—	0.25 ms	86
Fe_3O_4	0.3–10.6	561.2	10^{8}	0.9/0.7 s	209
$PtTe_2$	0.2–1.65	0.40	10^{12}	7.5/36.7 μs	210
Cr_2S_3	0.52–1.55	3	10^{9}	1.7/1.65 s	211
Bi_2Se_3	0.33–1.55	2.7	10^{10}	0.5 s	212
In_2Se_3	405–940	9.8×10^{4}	3.3×10^{13}	30 ms	213
WSe_2/Gr/MoS_2	400–2400	10^{4}	10^{15}	53.6/30.3 μs	214
PbS/MoS_2	400–1500	6×10^{5}	7×10^{14}	0.3–0.4 s	215
BP	310–1240	9×10^{4}	3×10^{13}	3.0/7.8 s	168
InSe	254–850	10^{4}	10^{13}	5.0/8.0 ms	216
MoS_2/h-BN/Gr	400–885	180	2.6×10^{13}	0.23/0.25 s	217
MoS_2/Si	420–1064	0.3	10^{13}	3/40 μs	218
PbSe/TiO_2/Gr	350–1700	0.506	3×10^{13}	0.68/0.70 s	185
WSe_2 sputtered	500–900	1.8×10^{5}	3×10^{14}	23 ms	219

red wavelengths of 1550 nm and demonstrated a fast response time of approximately 3 μs, as shown in Fig. 9(f), and a responsivity of 1.3 A W^{-1}.[196] The high-speed rise/fall times of different 2D materials are shown in Table 6.

In their most recent study, Zhang *et al.* developed a high-performance unipolar barrier detector using a vdW heterojunction composed of black arsenic phosphorus (b-AsP), MoS_2, and BP.[220] The device demonstrates a broad spectral response, ranging from 520 nm to 4.6 μm, achieving a remarkable blackbody detectivity of 2.7×10^{10} cm Hz$^{-1/2}$ W^{-1} in the mid-infrared region at room temperature that highlights the potential of these barrier devices for mid-infrared detection applications. A structural diagram and an optical image of the detector based on the b-AsP/MoS_2/BP vdWH are shown in Fig. 10(a and b). EDS mapping and a cross-sectional TEM image of the b-AsP/MoS_2/BP vdWH, with distinct color-coded regions in the EDS maps, representing the spatial distribution of the constituent elements phosphorus (P), arsenic (As), molybdenum (Mo), sulfur (S), and oxygen (O), are shown in Fig. 10(c). HRTEM images of the b-AsP/MoS_2/BP vdWH interface show a thin amorphous layer at the b-AsP/MoS_2 interface potentially from the oxidation of b-AsP during device fabrication, as shown in Fig. 10(d). The bandgap tunability of TMDCs plays a critical role in the spectral response and performance of photodetectors. The spectral response indicates a detector's sensitivity across various wavelengths and is governed by the bandgap of a material, which sets the minimum photon energy required for absorption. TMDCs exhibit the unique property of a layer-dependent bandgap, where the bandgap energy varies significantly with the number of atomic layers.[221,222] This tunability enables precise control over the spectral range of detection by engineering the number of layers. Moreover, combining different TMDCs or stacking layers of varying thicknesses in heterostructures enables multi-spectral detection. Beyond structural control, external modulation through strain or electric fields can dynamically adjust the bandgap, allowing real-time tuning of the spectral response for advanced applications like adaptive IR imaging or selective gas sensing. This strong correlation between bandgap engineering and spectral tunability highlights the versatility of TMDCs in enabling high-performance, wavelength-specific photodetectors.[223] Photons absorbed by the b-AsP layer in the band structure create electron–hole pairs. The electric field separates these pairs, and the electrodes collect them, leading to a photocurrent. The band structure of the b-AsP/MoS_2/BP vdWH pBp barrier detector under reverse bias is shown in Fig. 10(e). However, holes generated at the BP contact layer encounter a barrier that prevents their flow and leads to recombination with electrons, which effectively reduces the dark current while enabling efficient photocurrent collection under reverse bias.

The I–V characteristics of the detector under different light wavelengths, from 520 to 1650 nm, are presented in Fig. 10(f), showing both dark and illuminated states with an effective power of 4 μW. The power-dependent responsivity (R) of the device is illustrated in Fig. 10(g). The data reveal a gradual increase in responsivity from 0.34 to 0.89 A W^{-1} as the wavelength extends from the visible to the short-wave infrared range. Fig. 10(h and i) shows the relationship between responsivity and photocurrent of the device, where a sub-ideal exponent suggests the presence of interface defects. Fig. 10(j) demonstrates the time response of the detector to pulsed optical excitation at different reverse bias voltages. It shows that while the current increases with bias, the dark current also rises, highlighting the need to optimize the bias voltage for balance between sensitivity and noise. Thorough examin-

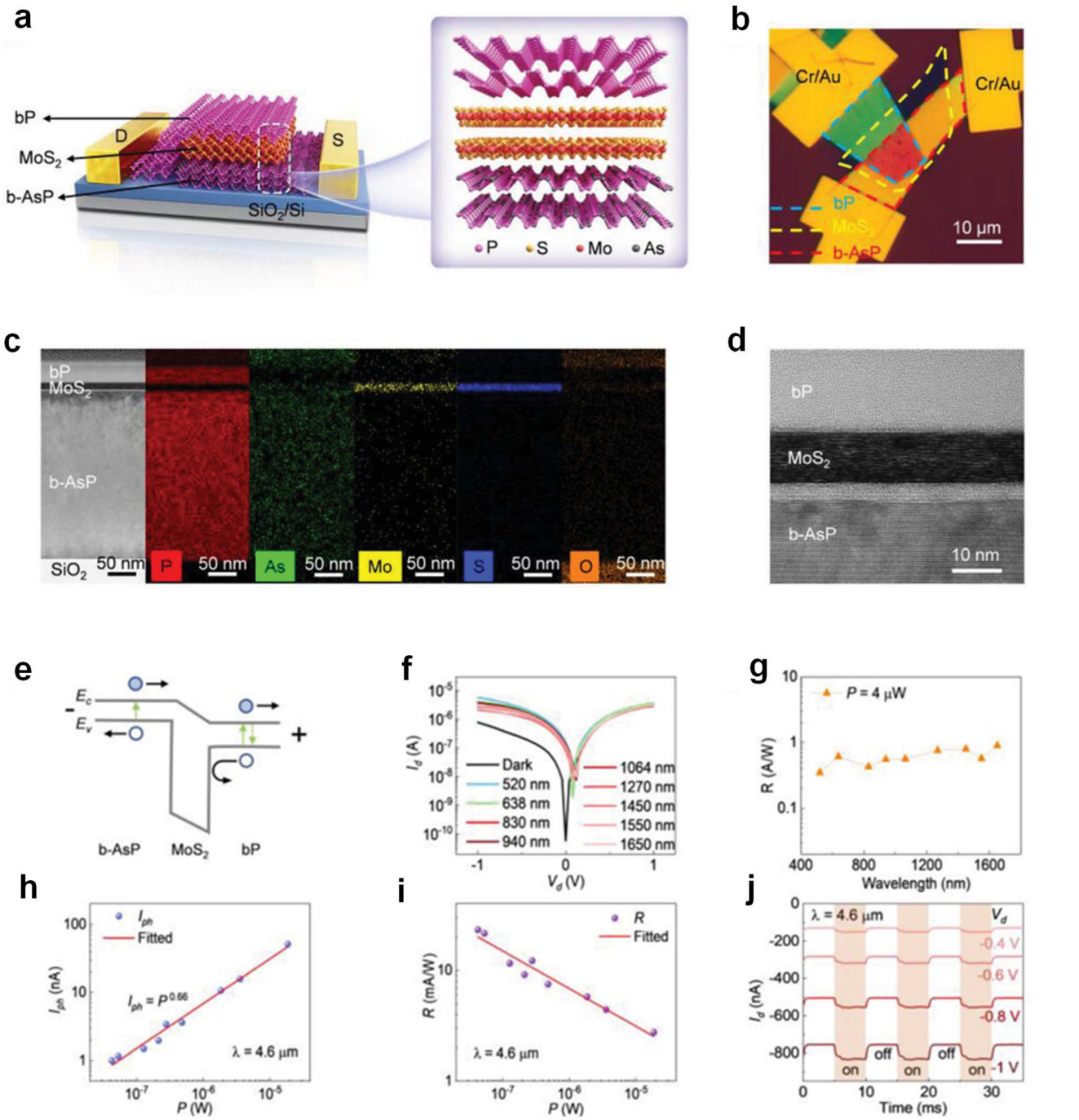

Fig. 10 Broad spectral unipolar barrier detector. (a and b) Schematic and optical image of the b-AsP/MoS_2/BP vdWH photodetector. (c) EDS analysis indicating the distribution of P, As, Mo, S, and O. (d) TEM analysis of the b-AsP/MoS_2/BP vdWHs with a scale bar of 10 nm. (e) Energy band structure of the b-AsP/MoS_2/BP van der Waals heterojunction device. (f) *I*–*V* curves under light pulses of various wavelengths. (g) Variation in responsivity as a function of wavelength at a fixed power of 4 μW. (h and i) Power dependent photocurrent and responsivity at a wavelength of 4.6 μm. (j) Time-dependent photoresponse under various biasing voltages at a wavelength of 4.6 μm, adapted with permission from Wiley.[220]

ation of the b-AsP/MoS_2/BP van der Waals heterojunction device performance highlights how well this heterojunction works to improve infrared detection. Despite challenges such as defect-related effects and increasing dark current with bias, the findings provide valuable insights for optimizing and advancing IR photodetector technologies.

8. Applications

Infrared photodetectors are widely utilized for their capability to detect light beyond the visible spectrum. Some prominent applications include night vision, security and surveillance, fire detection, medical imaging, environmental monitoring,

spectroscopy and communication. In this section, we discuss some prominent applications of IR photodetectors.

8.1 Shortwave infrared light detection for medical imaging

There is significant demand for technologies that can capture images in the shortwave infrared (SWIR) region over a large area. Upconversion imagers are particularly attractive for this purpose because they offer a combined solution. These images can both sense light in the SWIR spectrum and convert it into a visible image, all within a single compact device.[81,224] This eliminates the need for pixelation, which is a complex and expensive process traditionally used in SWIR cameras. A recent study by Li *et al.* demonstrated a novel organic upconversion imager for shortwave infrared (SWIR) light detection. This imager achieves efficient conversion of SWIR light of up to 1400 nm into a visible image, enhancing capabilities for both human and machine vision. The design incorporates special layers to minimize energy loss and improve light conversion efficiency. The imager demonstrates a performance comparable to that of cutting-edge organic infrared photodiodes, with an EQE of up to 35% under a low voltage and a promising bandwidth response. Additionally, the large active area of approximately 2 cm^2 makes it suitable for multiple applications, such as imaging through obstacles like smog, object inspection, and even simultaneously capturing blood vessel location and blood flow information. An up-conversion imager schematic is shown in Fig. 11(a), featuring a design with optical and dual electronic readouts. The device can both convert incoming light into electrical signals and directly emit visible light for visual observation. SWIR light was directed onto a hand, and the imager upconverted the reflected light. The upconverted image revealed details of the fingertip, including the white edge and cuticle of the fingernail. This capability is due to the high absorption of SWIR light by water. The human body is composed of a significant amount of water, including the tissues beneath the skin's surface. The imager was further employed to visualize blood vessels within the hand. These blood vessels appeared darker in the image compared to the surrounding tissue because hemoglobin within red blood cells strongly absorbed SWIR light. This characteristic absorption property of hemoglobin makes SWIR imaging a potentially valuable tool for biometric authentication techniques based on vasculature patterns, as shown in Fig. 11(b).[225] Another study by Yokota *et al.* introduced a novel conformable imager for biometric authentication and vital sign monitoring. This innovative device combines thin-film transistor circuits made from polycrystalline silicon with highly sensitive near-infrared organic photodiodes. This combination creates a flexible imager with an impressive resolution of 508 pixels per inch, a fast frame rate of 41 frames per second, and an incredibly thin profile of 15 μm. The imager boasts exceptional low-noise performance, capable of reading out tiny photocurrents, *i.e.*, less than 10 pA. When gently pressed against the skin, it can capture static biometric data, such as fingerprints and vein imagery, and it can also dynamically map pulse waves by electronically selecting the optimal measurement location based on real-time analysis of the signal distribution across the skin surface. A visual representation of the imager is shown in Fig. 11(c). For better imaging resolution, the imager is used with a resolution chart containing 15 lines and line width spacing of 50 μm, which confirms a high resolution of 508 pixels per inch (ppi) with no visible defects and excellent uniformity that are necessary for accurately extracting features like fingerprints and vein patterns for biometric authentication. The images of finger vein patterns in transmission mode using an optical system are shown in Fig. 11(d). The images reveal vein characteristics, including branching points, branching angles, and the number of veins, all of which are important factors for reliable vein-based authentication for medical imaging.

8.2 Infrared multi-spectral imaging for low-cost and scalable devices

Infrared multispectral imaging offers a powerful approach for capturing detailed information across multiple infrared wavelengths.[227,228] This technique is gaining significant interest due to its potential applications in various fields. However, a key hurdle hindering its widespread adoption is the high cost associated with conventional detectors based on epitaxial semiconductors. Epitaxial growth processes involve depositing thin, crystalline layers of a material onto a substrate, which can be expensive and complex to implement. A promising approach for overcoming the limitations of traditional infrared detectors was presented by Tang *et al.* In their work, they developed a two-terminal photodetector based on stacked colloidal quantum dots (CQDs). This novel design offers a bias-switchable spectral response in which the detector can be tuned to sense light in two distinct infrared bands by adjusting the applied voltage. The key to this functionality lies in a vertically stacked structure containing two rectifying junctions arranged in a back-to-back arrangement. This configuration is achieved through a meticulously engineered doping process that ensures strong and stable spatial separation of charge carriers within the device. By precisely adjusting the magnitude and voltage polarity, the detector can swiftly alternate between sensing MWIR and SWIR light. The design of the dual-band detector incorporates two separate photodiodes, one sensitive to SWIR and the other to MWIR, as shown in Fig. 12(a). These photodiodes are arranged in an opposing n–p–n structure, using Ag_2Te and Bi_2Se_3 materials for the p and n layers, respectively. The SWIR photodiode is layered above the MWIR photodiode with light entering from the top surface. This configuration maximizes light absorption within both layers, enabling efficient detection across the two infrared bands. A single-pixel scanning imaging system with a BaF_2 lens was built to visually demonstrate the detector's dual-band capability by scanning a projected image across its surface. By carefully switching the applied bias voltage, the system can achieve either active SWIR imaging or passive MWIR imaging. An external light source, such as a tungsten lamp, is required to activate the SWIR. A comparison of SWIR imaging and visible images of various solvents contained within glass and glass

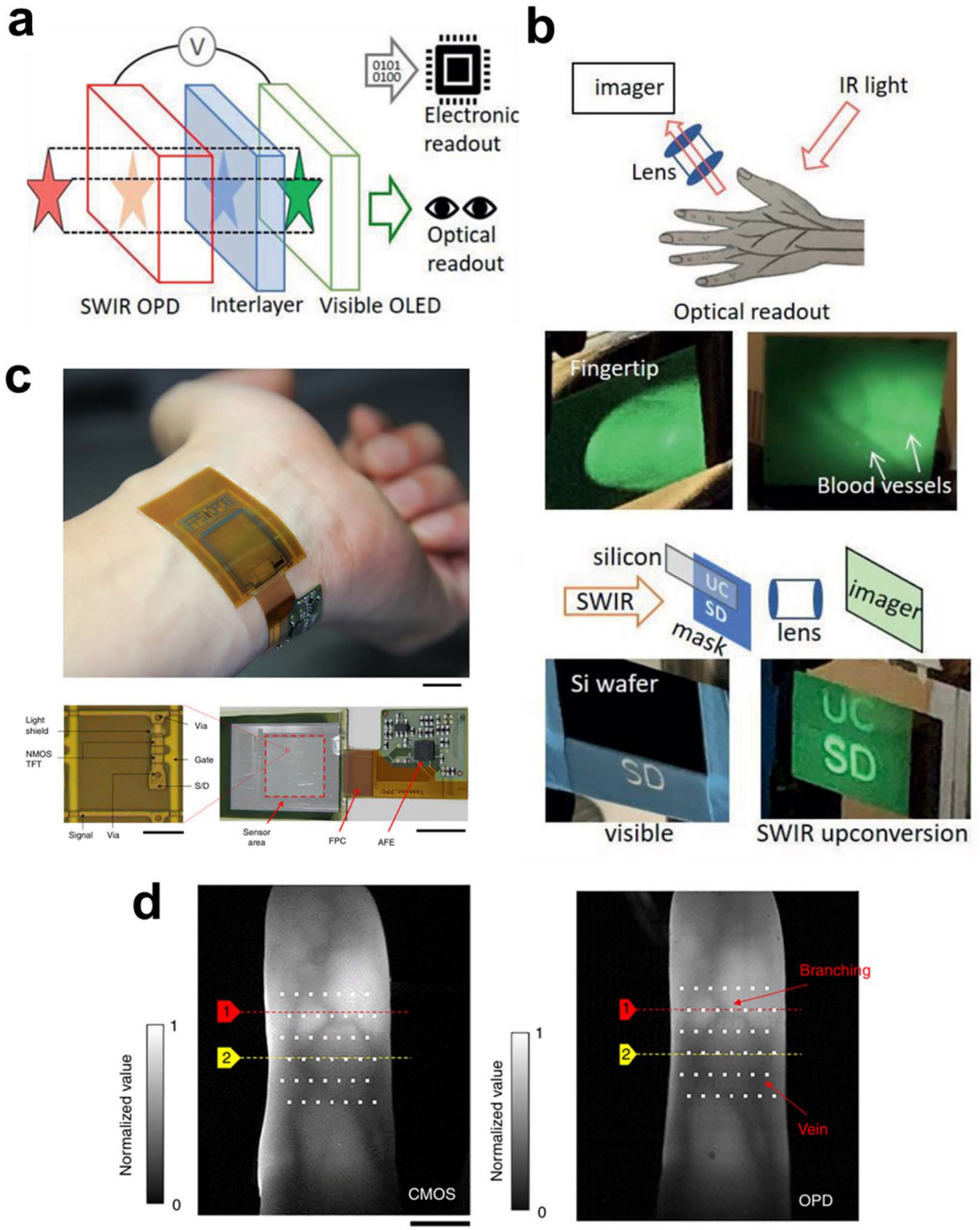

Fig. 11 IR light detection for medical imaging. (a and b) Illustration of the up-conversion imager with optical and electronic dual readouts, up-conversion imager detected reflected infrared light from a human hand, revealing fingertip and blood vessels. Imager with photocurrent modulation to a person's heartbeat demonstrates non-contact photoplethysmography (PPG) imaging, and letters under a silicon wafer opaque to visible light but transparent to SWIR, adapted with permission from Wiley.[225] (c) Integration of polycrystalline silicon thin-film transistor (TFT) circuits with sensitive NIR organic photodiodes. (d) Finger vein imaging: images on the right and left obtained using conformable and CMOS imagers, respectively. A 2D array of 0.3 mm square white dots is overlaid on the images to safeguard personal data from biometric identification, with a horizontal pitch of 0.9 mm and a vertical pitch of 1.5 mm. (c and d) Adapted with permission of Nature Springer.[226]

filled with water in SWIR and MWIR imaging is shown in Fig. 12(b). Notably, the solvents, which appear transparent in the visible image, exhibit distinct features in the SWIR image. This difference arises from the unique absorption patterns of the solvents at specific SWIR wavelengths caused by the vibration of molecules. Another study by Yu *et al.* explored a promising approach for infrared imaging utilizing high-gain infrared-to-visible up-conversion light-emitting phototransis-

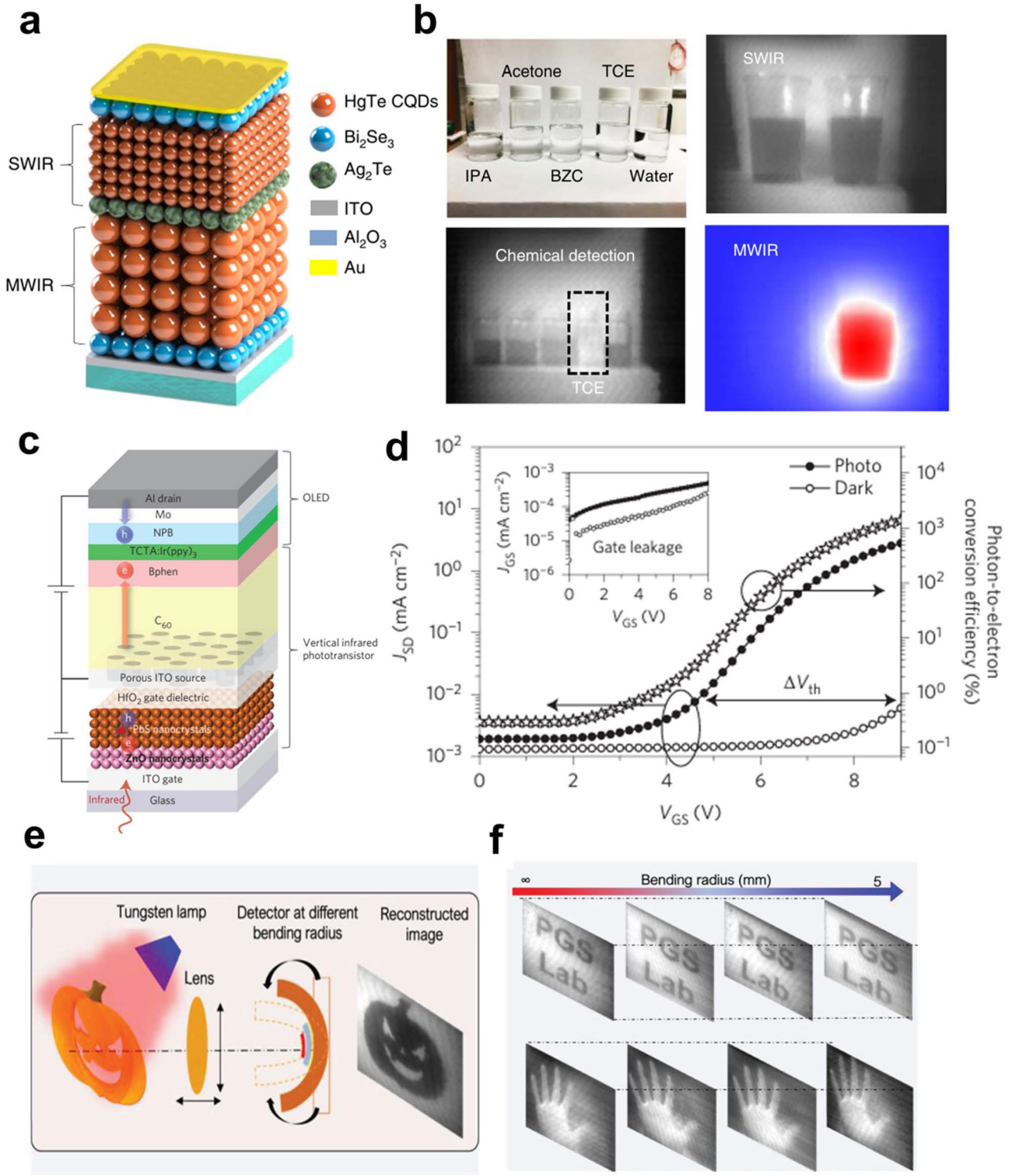

Fig. 12 IR multi-spectral imaging for low cost and scalable devices. (a) Dual-band imaging device using HgTe colloidal quantum dots (CQDs) and V_{ds} applied between the Au and indium tin oxide (ITO) contacts. (b) Images of various solvents in the visible and SWIR range, as well as SWIR and MWIR images of cold and hot water, with the MWIR captured at 85 K. (a and b) Adapted with permission from Nature Springer.[229] (c) Schematic diagram of a phosphorescent OLED and a vertical phototransistor with an infrared-sensitive gate utilizes colloidal PbS nanocrystals, and the ITO layer serves as the working electrode. (d). Transfer curve with infrared illumination (filled circles) and without (open circles) at λ = 1042 nm and 240 μW cm^{-2} with V_{ds} = 3 V indicates efficient photon to electron conversion. (c and d) Adapted with permission from Nature Springer.[23] (e and f) Setup of flexible CQD photovoltaic detectors with an enhanced resonant cavity for infrared imaging. A tungsten lamp provides active infrared illumination, and images are taken at varying bending radii of the flexible detectors, adapted with permission from Wiley.[230]

tors. The device integrates an infrared quantum dot detector and an organic light-emitting diode (OLED) into a single device, as shown in Fig. 12(c). The design offers an intriguing potential pathway toward achieving low-cost, pixel-free infrared imaging systems, since the infrared quantum dot photodetector within the device is sensitive to incoming infrared light. Upon absorbing these infrared photons, the photodetector generates an electrical current that is efficiently converted into visible light by the OLED component, essentially achieving upconversion from the infrared to the visible spectrum, which eliminates the need for traditional pixelated detectors, potentially leading to simpler and more cost-effective infrared imaging solutions. An analysis of the device's electrical behavior reveals a key mechanism for its functionality, as shown in Fig. 12(d). When no infrared light is present, a minimal current of 10^{-3} mA cm^{-2} flows through the device until the gate voltage reaches 8 V. However, under infrared illumination, the gate voltage required to achieve the same current level is significantly reduced. This shift in the curves represents the substantial enhancement of the photocurrent generated by infrared light compared to the dark current. A high photon-to-electron conversion efficiency characterizes this efficient conversion of infrared light into electrical current. Another study by Tang *et al.* proposes a promising approach for infrared electronic eye cameras. These cameras offer wider fields of view and simpler designs compared to traditional systems. The device includes flexible CQD detectors made from mercury telluride (HgTe) because of its fast response, flexibility, high sensitivity and wide spectral range. A Fabry–Perot resonant cavity is used to improve light absorption. Fig. 12(e) shows the setup for infrared imaging using a flexible detector while Fig. 12(f) shows images captured with different bending radii. This achievement of integrating high-performance SWIR detectors onto flexible substrates opens exciting possibilities for new-generation infrared electronic eye cameras. The combination of high-resolution imaging and adaptability to diverse surfaces makes these advanced cameras ideal for night vision and surveillance, medical imaging, and industrial inspection.

8.3 High frequency and ultra-fast infrared photodetectors

Infrared light detection plays an important role in numerous modern technologies, and advancements in photoelectric materials have continuously driven its development. 2D materials emerge as a promising platform for next-generation infrared photodetectors due to their distinctive electronic structures, extreme confinement of electrons within their atomic layers, and strong interactions with light. However, achieving an ideal infrared detector that simultaneously offers a fast response, high sensitivity, and air stability remains a challenge.[231,232] A recent study by Yin *et al.* explored high-performance and ultrafast infrared detectors based on two-dimensional Bi_2O_2Se crystals.[233] The Bi_2O_2Se-based photodetector exhibits a high sensitivity of 65 A W^{-1} at a wavelength of 1200 nm and an ultrafast photoresponse of 1 picosecond (ps) at room temperature, which signifies the capability to detect and respond to rapidly changing infrared signals. Bi_2O_2Se is a promising 2D material consisting of alternating Bi_2O_2 layers and Se layers—each layer has an approximate thickness of 0.61 nm—exhibiting high carrier mobility and air stability.[234] The device exhibits a remarkable responsivity of 65 A W^{-1}, which shows its capability to effectively distinguish weak infrared signals from background noise at wavelengths of 1200 nm and 1550 nm, as shown in Fig. 13(a). The photoresponse time of the detector determines the inherent bandwidth limitation due to the material's properties, device design, and stray capacitance. The photocurrent is measured as a function of the time delay between two ultrashort laser pulses under zero bias voltage. When the time delay is minimal, the photocurrent is at its lowest because the first excitation pulse does not have enough time to generate a current before it overlaps with the second excitation pulse. This overlap leads to a nonlinear response in the photocurrent in the form of an observed dip. The performance of Bi_2O_2Se compared with graphene is shown in Fig. 13(b). As the time delay increases, excitation from the two pulses becomes independent. This enables the detector to respond to each pulse effectively, leading to a rise in the photocurrent towards a maximum value as the normalization point.[190,235] In another study, Li *et al.* explored a promising approach for ultra-fast infrared photodetectors. The device structure consists of p–g–n junctions using a layered two-dimensional (2D) material heterostructure of molybdenum ditelluride ($MoTe_2$), graphene, and tin disulfide (SnS_2). The key advantage of utilizing 2D TMDCs lies in their ability to be stacked layer-by-layer, which eliminates the challenges associated with traditional heteroepitaxy methods.[236] These processes involve stacking different materials on top of one another, which can be constrained by lattice mismatch. Fabrication of the device involved a dry transfer method and combined h-BN as the outmost layers, graphene (Gr) as an interlayer, and molybdenum ditelluride ($MoTe_2$), a p-type material with a bandgap of approximately 1.0 eV, and tin disulfide (SnS2) as an n-type semiconductor with a bandgap of approximately 2.2 eV. The stacked structure and an optical image of device are shown in Fig. 13(c). The photocurrent response of the device characterized by rise and fall times shows a maximum photocurrent between 10% and 90% upon light switching ON and OFF, respectively. The rise and fall times exhibited asymmetry under light with varying excitation wavelengths. Under 405 nm light, the rise time was 17.6 ms, while the fall time was significantly slower at 72.3 ms. In NIR light at 1064 nm, the rise and fall times were more symmetrical, at 24.1 ms and 28.6 ms, respectively. The photocurrent response of the device under different light illumination, with rise and fall times, is shown in Fig. 13(d). The fast and symmetrical response observed under NIR illumination is due to the built-in electric field within the p–n junction, which effectively reduces the trapping of photogenerated carriers, and the zero-bandgap graphene layer acts as an efficient interfacial contact between $MoTe_2$ and SnS_2, which minimizes interface traps and facilitates the rapid transport of carriers separated by the built-in field.[237]

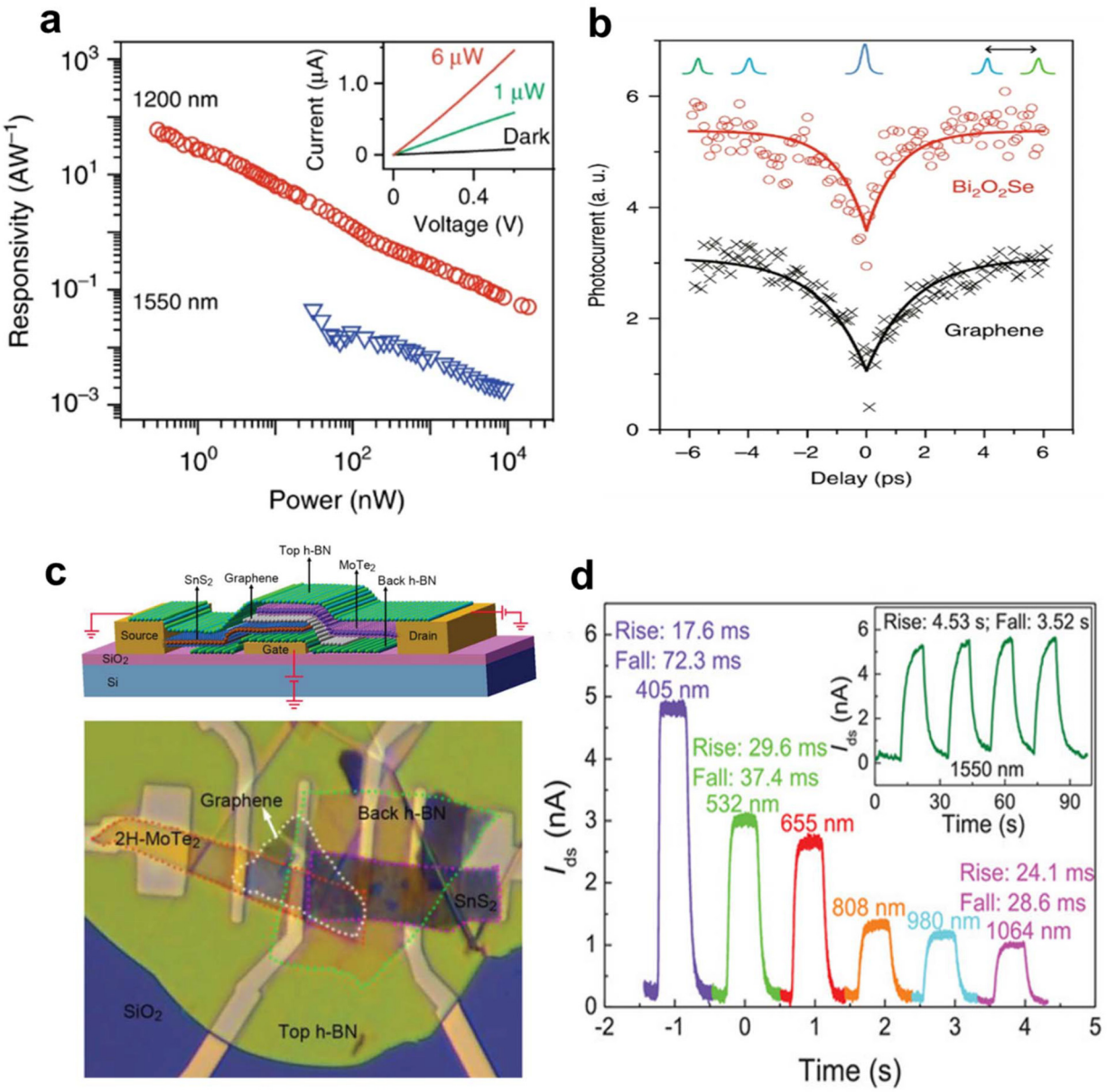

Fig. 13 High frequency and ultrafast IR detectors. (a) Bi_2O_2Se photodetector showing a high responsivity of 65 A W^{-1} at V_{ds} = 0.6 V and wavelengths of 1200 nm and 1500 nm. (b) Time-resolved photocurrent analysis shows, at very short delay times, the first excitation pulse does not fully convert into current before encountering the second pulse, leading to a sublinear current and dip at zero delay. Longer delay times enable independent excitation by each pulse, resulting in the maximum voltage used as the normalization value. Black crosses and red circles represent the graphene and Bi_2O_2Se photodetectors, respectively, with solid lines indicating exponential fits. (a and b) Adapted with permission from Nature Springer.[233] (c) Schematic diagram and optical image of h-BN/$MoTe_2$/Gr/SnS_2/h-BN vdWHs. (d) Photocurrent response measured at 0.5 V bias across wavelengths of 405–1064 nm with optical powers in the range of 42–62 nW. The inset shows the temporal photocurrent response at a wavelength of 1550 nm. The fast and symmetrical response observed under NIR illumination is because of the built-in electric field present within the p–n junction, which effectively minimizes carrier trapping, and the zero-bandgap graphene layer acts as an efficient interfacial contact between $MoTe_2$ and SnS_2. (c and d) Adapted with permission from Wiley.[238]

9. Challenges and future outlook

This review explored recent progress in infrared (IR) photodetectors built using two-dimensional (2D) materials. These materials, due to their atomically thin structure, can absorb a wide range of light, from ultraviolet (UV) to terahertz (THz) frequencies.[239,240] However, due to the thin structure, it presents the challenge of weak light absorption because the limited thickness leads to insufficient light capture, which results in a low EQE and detectivity. These materials are more vulnerable to defects due to their sharp nature and act as recombination centers, reducing the photogenerated carrier

lifetime and limiting the device performance. The refractive index of the underlying substrate is crucial for light absorption. A substrate with a lower refractive index enhances the absorption efficiency of the thin 2D layer by facilitating stronger light coupling. However, achieving a large area and uniform growth poses a challenge. Current methods, such as chemical vapor deposition (CVD) or transfer techniques, primarily result in small-scale samples.[241,242] Some high mobility 2D materials like BP suffer from instability under ambient conditions, which limits their long-term functionality. While some TMDCs have strong light–matter interactions, their inherently low carrier mobility hinders the overall performance of the device. These limitations highlight the need for further research to address these trade-offs and unlock the full potential of 2D materials for high-performance IR photodetectors. Creating high-performance infrared (IR) photodetectors with two-dimensional (2D) materials requires a comprehensive and multi-dimensional approach. Here, we discuss some approaches that can be used to increase the overall performance of next-generation IR detector devices.

9.1 Material optimization

(1) Material design and optimization: Exploring the size, shape, and thickness of 2D materials is essential to influence bandgaps for efficient light absorption within the desired IR range. Strategies such as using specific nanoribbons and quantum dot geometries or incorporating van der Waals heterostructures can further enhance absorption.[243,244] **(2) Hybrid material integration**: Combining 2D materials with other light-harvesting materials like quantum dots or carbon nanotubes presents a promising approach for enhanced light absorption.[245,246] **(3) Light trapping techniques**: Integrating plasmonic technologies that manipulate light at the nanoscale can be employed to improve light–matter interactions within the thin 2D layer.[247] **(4) Theoretical modeling**: Developing robust theoretical models is crucial for predicting the impact of various tuning strategies on the physical and optical properties of 2D materials. Techniques like chemical doping, mechanical strain, and optical and electrical gating can be simulated to optimize device function and performance.[248,249]

9.2 Device structure optimization

Beyond material optimization, investigating innovative device architectures can lead to further enhancements in performance. This discussion explores several strategies for advancing the next generation of IR detectors to boost overall performance. **(1) Cascade photodetectors**: Adding a light-absorbing layer with a strategically aligned bandgap within a p–n junction can enhance overall light absorption and could achieve a better balance between high quantum efficiency and a low dark current.[250,251] **(2) Minimizing transfer-induced defects**: The common dry transfer process for fabricating 2D material devices can introduce contaminants and defects at material interfaces. These defects act as recombination centers, reducing carrier lifetimes and hindering device performance. Research efforts are needed to develop new techniques for minimizing these transfer-induced issues.[252,253] **(3) Quantum well and superlattice integration**: Quantum well structures and superlattices exploit quantum confinement effects to tailor the band structure and enhance light–matter interactions within the 2D material and could be promising avenues for achieving high detectivity.[254] **(4) Scalable production**: Current methods for producing high-quality 2D materials and heterostructures often struggle with scalability. Achieving large-scale, uniform growth remains a significant challenge for realizing industrial applications.[255,256]

9.3 Accurate noise characterization for 2D material photodetectors

In high ON/OFF ratio devices, the significant difference between light and dark currents often leads to the operating current being ignored when calculating shot noise, which can result in a substantial overestimation of detectivity. This underestimation of light performance creates practical limitations for devices. As a result, some reported 2D material photodetectors, despite theoretically outperforming commercial detectors, struggle under natural light sources and black body radiation. Their intrinsic noise levels are much higher than those theoretically calculated, which limits their real-world applications.[257,258] Increasing the number of layers in a 2D material can directly improve light absorption. However, this also leads to a larger dark current, which degrades the SNR and detectivity. Therefore, finding the optimal thickness for each specific material is crucial for achieving the best overall performance. Despite current challenges, the increasing demand for high-sensitivity and reliable infrared (IR) detection technologies paves the way for a promising future for 2D material-based IR detectors. This next generation of technology holds immense potential to revolutionize the fields of night vision, optical communication, surveillance, remote sensing, environmental monitoring, and medical imaging.

10. Conclusion

This review has comprehensively explored the advancements in infrared (IR) photodetectors, with a particular focus on the potential of 2D materials and their vdW heterostructures. The discussion covers the evolution of IR photodetectors, from traditional materials with narrower bandgaps to the emergence of 2D materials, representing a significant leap forward in photodetection technology. This review examined various detection mechanisms, including photoconductive, photogating, photobolometric, photothermal, and photovoltaic effects, highlighting their relevance to the operation of 2D material-based IR detectors. This paper also discussed the potential of 2D materials, such as BP, InSe, and layered TMDCs, for use in IR photodetectors. These materials offer significant advantages, including high responsivity, specific detectivity, and photoconductive gain. They also address challenges like shot and thermal noise, making them promising candidates for advanced IR detection technologies.

The review also explores the diverse applications of 2D material-based IR photodetectors, including their use in medical imaging, multispectral imaging for low-cost devices, and high-frequency, ultra-fast detection systems. These applications demonstrate the versatility and potential impact of 2D materials on advancing IR photodetection technology. However, the field still faces several challenges, particularly in material and device structure optimization. Efforts are needed in material design, hybrid material integration, light trapping techniques, and accurate noise characterization to fully unlock the potential of these devices. Theoretical modeling and scalable production techniques will also play important roles in overcoming these challenges.

While significant progress has been made, further research and innovation are essential to address the remaining challenges and fully maximize the advantages of 2D materials for IR photodetection. This review aims to serve as a foundation for future studies and developments in this promising field, paving the way for the next generation of high-performance, scalable, and versatile IR photodetectors.

Author contributions

Muhammad Wajid Zulfiqar: investigation, formal analysis, validation, visualization, writing – original draft, writing – review & editing, conceptualization. Sobia Nisar: writing – original draft, visualization, validation, formal analysis, investigation, conceptualization, writing – review & editing. Ghulam Dastgeer: conceptualization, funding acquisition, project administration, methodology, supervision, writing – original draft, writing – review & editing. Muhammad Rabeel: writing – review & editing, validation, software, methodology. Hammad Ghazanfar: writing – review & editing, visualization, methodology, investigation. Awais Ali: writing – review & editing, visualization, validation, formal analysis, data curation. Muhammad Imran: writing – review & editing, visualization, methodology, investigation. Honggyun Kim: writing – review & editing, validation, software, resources, data curation. Deokkee Kim: supervision, funding acquisition, project administration, methodology, conceptualization, investigation, writing – review & editing.

Conflicts of interest

The authors declare no conflict of interest.

Abbreviations

0D	Zero-dimensional
1D	One-dimensional
2D	Two-dimensional
APD	Avalanche photodiode
BP	Black phosphorus
CQD	Colloidal quantum dot
EQE	External quantum efficiency
FET	Field effect transistor
FTIR	Fourier-transform infrared
GHz	Gigahertz
h-BN	hexagonal boron nitride
InSe	Indium selenide
IQE	Internal quantum efficiency
IR	Infrared
LIDAR	Light detection and ranging
LWIR	Long-wave infrared
MWIR	Mid-wave infrared
NEP	Noise equivalent power
OLED	Organic light emitting diode
PBE	Photobolometric effect
PCE	Photoelectric conversion efficiency
PEM	Photoelectromagnetic
PGE	Photogating effect
PTE	Photothermal effect
PVE	Photovoltaic effect
QD	Quantum dot
RMS	Root mean square
SNR	Signal-to-noise ratio
SWIR	Short-wave infrared
THz	Terahertz
TMDCs	Transition metal dichalcogenides
UV	Ultraviolet

Data availability

The data that support the findings of this study are available from the authors upon reasonable request.

Acknowledgements

This research is supported by the National Research Foundation (NRF) of Korea, funded by the Ministry of Science and ICT (RS-2024-00411969 & RS-2024-00468995). The authors extend their appreciation to the Deanship of Research and Graduate Studies at King Khalid University, Saudi Arabia, through Large Research Project under grant number RGP-2/527/46.

References

1 G. Dastgeer, *et al.*, Bipolar junction transistor exhibiting excellent output characteristics with a prompt response against the selective protein, *Adv. Funct. Mater.*, 2022, **32**(38), 2204781.
2 S. Nisar, *et al.*, Gate-assisted $MoSe_2$ transistor to detect the streptavidin via supporter molecule engineering, *Mater. Today Nano*, 2023, **24**, 100405.
3 L. Britnell, *et al.*, Strong Light-Matter Interactions in Heterostructures of Atomically Thin Films, *Science*, 2013, **340**(6138), 1311–1314.

4 K. Roy, *et al.*, Graphene–MoS_2 hybrid structures for multifunctional photoresponsive memory devices, *Nat. Nanotechnol.*, 2013, **8**(11), 826–830.
5 J. Bullock, *et al.*, Polarization-resolved black phosphorus/molybdenum disulfide mid-wave infrared photodiodes with high detectivity at room temperature, *Nat. Photonics*, 2018, **12**(10), 601–607.
6 G. Rao, *et al.*, Two-dimensional heterostructure promoted infrared photodetection devices, *InfoMat*, 2019, **1**(3), 272–288.
7 A. K. Geim and I. V. Grigorieva, van der Waals heterostructures, *Nature*, 2013, **499**(7459), 419–425.
8 F. Wang, *et al.*, Field-free switching of perpendicular magnetization by two-dimensional $PtTe_2$/WTe_2 van der Waals heterostructures with high spin Hall conductivity, *Nat. Mater.*, 2024, **23**(6), 768–774.
9 H. Qiu, *et al.*, Two-dimensional materials for future information technology: status and prospects, *Sci. China Inform. Sci.*, 2024, **67**(6), 160400.
10 S. Nisar, *et al.*, Chemically doped-graphene FET photodetector enhancement via controlled carrier modulation with an iron(III)-chloride, *Diamond Relat. Mater.*, 2024, **145**, 111089.
11 A. M. Afzal, *et al.*, Highly Sensitive, Ultrafast, and Broadband Photo-Detecting Field-Effect Transistor with Transition-Metal Dichalcogenide van der Waals Heterostructures of $MoTe_2$ and $PdSe_2$, *Adv. Sci.*, 2021, **8**(11), 2003713.
12 G. Dastgeer, *et al.*, Temperature-Dependent and Gate-Tunable Rectification in a Black Phosphorus/WS_2 van der Waals Heterojunction Diode, *ACS Appl. Mater. Interfaces*, 2018, **10**(15), 13150–13157.
13 Z. Zhang, *et al.*, Recent progress of microwave absorption motivated by metal single atoms anchored on two-dimensional materials, *Carbon*, 2025, **235**, 120095.
14 Z. Liu, *et al.*, Classification of Three Anesthesia Stages Based on Near-Infrared Spectroscopy Signals, *IEEE J. Biomed. Health Inf.*, 2024, **28**(9), 5270–5279.
15 H. Wang, *et al.*, A Physical-Constrained Decomposition Method of Infrared Thermography: Pseudo Restored Heat Flux Approach Based on Ensemble Bayesian Variance Tensor Fraction, *IEEE Trans. Ind. Inf.*, 2024, **20**(3), 3413–3424.
16 J. Qi, W. Qiao and Z. Y. Wang, Advances in Organic Near-Infrared Materials and Emerging Applications, *Chem. Rec.*, 2016, **16**(3), 1531–1548.
17 S. Huo, *et al.*, Negative Differential Resistance with Ultralow Peak-to-Valley Voltage Difference in Td-WTe_2/2H-MoS_2 Heterostructure, *Nano Lett.*, 2024, **24**(38), 11937–11943.
18 X. Xue, *et al.*, High-operating-temperature mid-infrared photodetectors via quantum dot gradient homojunction, *Light: Sci. Appl.*, 2023, **12**(1), 2.
19 W. Zhu and S. Dong, Exoplanet Statistics and Theoretical Implications, *Annu. Rev. Astron. Astrophys.*, 2021, **59**, 291–336.
20 X. Zhang, *et al.*, Dark Current Mechanisms and Suppression Strategies for Infrared Photodetectors Based on Two-Dimensional Materials, *Laser Photonics Rev.*, 2024, **18**(5), 2300936.
21 T. Mueller, F. Xia and P. Avouris, Graphene photodetectors for high-speed optical communications, *Nat. Photonics*, 2010, **4**(5), 297–301.
22 H. Huang, *et al.*, Ferroelectric polymer tuned two dimensional layered MoTe 2 photodetector, *RSC Adv.*, 2016, **6**(90), 87416–87421.
23 H. Yu, *et al.*, High-gain infrared-to-visible upconversion light-emitting phototransistors, *Nat. Photonics*, 2016, **10**(2), 129–134.
24 P. Martyniuk, *et al.*, Infrared avalanche photodiodes from bulk to 2D materials, *Light: Sci. Appl.*, 2023, **12**(1), 212.
25 M. Dai, *et al.*, Long-wave infrared photothermoelectric detectors with ultrahigh polarization sensitivity, *Nat. Commun.*, 2023, **14**(1), 3421.
26 T. Zhang, *et al.*, Six-arm Stellat Dendritic-PbS Flexible Infrared Photodetector for Intelligent Healthcare Monitoring, *Adv. Mater. Technol.*, 2022, **7**(8), 2200250.
27 W. Herschel, XIV. Experiments on the refrangibility of the invisible rays of the sun, *Philos. Trans. R. Soc. London*, 1800, **90**, 284–292.
28 R. A. Smith, F. E. Jones and R. P. Chasmar, The detection and measurement of infra-red radiation, *Science*, 1968, 846.
29 P. W. Kruse, L. D. McGlauchlin and R. B. McQuistan, *Elements of infrared technology: Generation, transmission and detection*, Wiley, New York, 1962.
30 E. S. Barr, Historical survey of the early development of the infrared spectral region, *Am. J. Phys.*, 1960, **28**(1), 42–54.
31 T. Case, Notes on the change of resistance of certain substances in light, *Phys. Rev.*, 1917, **9**(4), 305.
32 R. Cashman, Film-type infrared photoconductors, *Proc. IRE*, 1959, **47**(9), 1471–1475.
33 P. R. Norton, *Infrared detectors in the next millennium. in Infrared Technology and Applications XXV*, SPIE, 1999.
34 X.-H. Li, *et al.*, Narrow-bandgap materials for optoelectronics applications, *Front. Phys.*, 2021, **17**(1), 13304.
35 T. C. McGill and D. A. Collins, Prospects for the future of narrow bandgap materials, *Semicond. Sci. Technol.*, 1993, **8**(1S), S1–S5.
36 Z. Lin, *et al.*, 2D materials advances: from large scale synthesis and controlled heterostructures to improved characterization techniques, defects and applications, *2D Mater.*, 2016, **3**(4), 042001.
37 M. S. Choi, *et al.*, Chemical Dopant-Free Doping by Annealing and Electron Beam Irradiation on 2D Materials, *Adv. Electron. Mater.*, 2021, **7**(10), 2100449.
38 A. Rogalski, Infrared detectors: an overview, *Infrared Phys. Technol.*, 2002, **43**(3), 187–210.
39 N. Li, *et al.*, Solution-processable infrared photodetectors: Materials, device physics, and applications, *Mater. Sci. Eng., R*, 2021, **146**, 100643.

40 G. Dastgeer, *et al.*, Gate modulation of the spin current in graphene/WSe_2 van der Waals heterostructure at room temperature, *J. Alloys Compd.*, 2022, **919**, 165815.
41 G. Dastgeer, *et al.*, Atomically engineered, high-speed non-volatile flash memory device exhibiting multibit data storage operations, *Nano Energy*, 2024, **119**, 109106.
42 S. Nisar, *et al.*, A novel biosensing approach: improving SnS_2 FET sensitivity with a tailored supporter molecule and custom substrate, *Adv. Sci.*, 2023, **10**(33), 2303654.
43 H. Z. Gul, *et al.*, Semimetallic Graphene for Infrared Sensing, *ACS Appl. Mater. Interfaces*, 2019, **11**(21), 19565–19571.
44 Z. Wang, *et al.*, Self-powered infrared detection using a graphene oxide film, *J. Mater. Chem. A*, 2020, **8**(18), 9248–9255.
45 H. Jiao, *et al.*, HgCdTe/black phosphorus van der Waals heterojunction for high-performance polarization-sensitive midwave infrared photodetector, *Sci. Adv.*, 2022, **8**(19), eabn1811.
46 X. Chen, *et al.*, Widely tunable black phosphorus mid-infrared photodetector, *Nat. Commun.*, 2017, **8**(1), 1672.
47 Y. Zhu, *et al.*, Non-volatile 2D MoS_2/black phosphorus heterojunction photodiodes in the near- to mid-infrared region, *Nat. Commun.*, 2024, **15**(1), 6015.
48 D. Wu, *et al.*, Phase-controlled van der Waals growth of wafer-scale 2D $MoTe_2$ layers for integrated high-sensitivity broadband infrared photodetection, *Light: Sci. Appl.*, 2023, **12**(1), 5.
49 Q. Ju, *et al.*, Infrared Interlayer Excitons in Twist-Free $MoTe_2$/MoS_2 Heterobilayers, *Adv. Mater.*, 2024, **36**(35), 2404371.
50 Y. Yildiz and M. Nalbant, A review of cryogenic cooling in machining processes, *Int. J. Mach. Tools Manuf.*, 2008, **48**(9), 947–964.
51 L. Anatychuk and L. Vikhor, The limits of thermoelectric cooling for photodetectors, *J. Thermoelectr.*, 2013, **5**, 54–58.
52 A. Rogalski, Infrared detectors: status and trends, *Prog. Quantum Electron.*, 2003, **27**(2), 59–210.
53 I. K. Kikoin and S. D. Lazarev, Photoelectromagnetic effect, *Sov. Phys. Usp.*, 1978, **21**(4), 297.
54 T. Manouras and M. Vamvakaki, Field responsive materials: photo-, electro-, magnetic-and ultrasound-sensitive polymers, *Polym. Chem.*, 2017, **8**(1), 74–96.
55 J. Shim, *et al.*, Room-temperature waveguide-integrated photodetector using bolometric effect for mid-infrared spectroscopy applications, *Light: Sci. Appl.*, 2025, **14**(1), 125.
56 M. Shen, *et al.*, Enhanced Pyroelectric Response in Quenched BNT–Based Lead–Free Ferroelectrics for Uncooled Infrared Detection, *Adv. Funct. Mater.*, 2025, 2423055.
57 S.-J. Wang, *et al.*, Doped organic thermoelectric short wavelength infrared detectors, *Sci. Adv.*, 2025, **11**(18), eadt0006.
58 A. Murros, *et al.*, Infrared bolometers based on 40 nm-Thick Nano-Thermoelectric silicon membranes, *Infrared Phys. Technol.*, 2025, 105720.
59 P. Zhang, G. Wang and H. Yu, Ultraviolet–visible–near–infrared light–responsive soft materials: Fabrication, photomechanical deformation and applications, *Responsive Mater.*, 2024, **2**(3), e20240016.
60 B. Li, *et al.*, Efficient and stable near-infrared InAs quantum dot light-emitting diodes, *Nat. Commun.*, 2025, **16**(1), 2450.
61 G. E. Stillman and C. M. Wolfe, Chapter 5 Avalanche Photodiodes**This work was sponsored by the Defense Advanced Research Projects Agency and by the Department of the Air Force, in *Semiconductors and Semimetals*, ed. R. K. Willardson and A. C. Beer, Elsevier, 1977, pp. 291–393.
62 J. C. Campbell, *et al.*, Recent advances in avalanche photodiodes, *IEEE J. Sel. Top. Quantum Electron.*, 2004, **10**(4), 777–787.
63 S. Ogawa and M. Kimata, Wavelength-or polarization-selective thermal infrared detectors for multi-color or polarimetric imaging using plasmonics and metamaterials, *Materials*, 2017, **10**(5), 493.
64 P. Jin, *et al.*, Realizing nearly-zero dark current and ultra-high signal-to-noise ratio perovskite X-ray detector and image array by dark-current-shunting strategy, *Nat. Commun.*, 2023, **14**(1), 626.
65 B. Wang and J. Mu, High-speed Si-Ge avalanche photodiodes, *PhotoniX*, 2022, **3**(1), 8.
66 X. Xuan, Joule heating in electrokinetic flow, *Electrophoresis*, 2008, **29**(1), 33–43.
67 H. Fangohr, *et al.*, Joule heating in nanowires, *Phys. Rev. B: Condens. Matter Mater. Phys.*, 2011, **84**(5), 054437.
68 S. Nisar, *et al.*, A Novel Biosensing Approach: Improving SnS_2 FET Sensitivity with a Tailored Supporter Molecule and Custom Substrate, *Adv. Sci.*, 2023, **10**(33), 2303654.
69 Z. Qiu, *et al.*, Giant gate-tunable bandgap renormalization and excitonic effects in a 2D semiconductor, *Sci. Adv.*, 2019, **5**(7), eaaw2347.
70 H. Fang and W. Hu, Photogating in low dimensional photodetectors, *Adv. Sci.*, 2017, **4**(12), 1700323.
71 J. Zha, *et al.*, Infrared Photodetectors Based on 2D Materials and Nanophotonics, *Adv. Funct. Mater.*, 2022, **32**(15), 2111970.
72 M. Long, *et al.*, Progress, Challenges, and Opportunities for 2D Material Based Photodetectors, *Adv. Funct. Mater.*, 2019, **29**(19), 1803807.
73 W. L. Zhen, *et al.*, Broadband photoresponse arising from photo-bolometric effect in quasi-one-dimensional $Ta_2Ni_3Se_8$, *J. Phys.: Condens. Matter*, 2022, **34**(25), 255303.
74 Y. Zhang, *et al.*, Highly Sensitive and Ultra-Broadband VO_2(B) Photodetector Dominated by Bolometric Effect, *Nano Lett.*, 2022, **22**(1), 485–493.
75 M. Cutler and N. F. Mott, Observation of Anderson localization in an electron gas, *Phys. Rev.*, 1969, **181**(3), 1336.
76 A. Rogalski, HgCdTe infrared detector material: history, status and outlook, *Rep. Prog. Phys.*, 2005, **68**(10), 2267.
77 J. C. Song, *et al.*, Hot carrier transport and photocurrent response in graphene, *Nano Lett.*, 2011, **11**(11), 4688–4692.

78 K.-J. Tielrooij, *et al.*, Generation of photovoltage in graphene on a femtosecond timescale through efficient carrier heating, *Nat. Nanotechnol.*, 2015, **10**(5), 437–443.
79 X. Lu, *et al.*, Progress of Photodetectors Based on the Photothermoelectric Effect, *Adv. Mater.*, 2019, **31**(50), 1902044.
80 G. Dastgeer, *et al.*, A review on recent progress and challenges in high-efficiency perovskite solar cells, *Nano Energy*, 2024, **132**, 110401.
81 S. Nisar, *et al.*, 2D Materials in Advanced Electronic Biosensors for Point-of-Care Devices, *Adv. Sci.*, 2024, 2401386.
82 S. Nisar, *et al.*, $MoTe_2$ field-effect transistor for the rapid detection of streptavidin via engineered support construct, *ACS Appl. Electron. Mater.*, 2023, **5**(10), 5714–5721.
83 M. W. Zulfiqar, *et al.*, Advancements in van der Waals Heterostructures Based on 2D Semiconductor Materials, *Arabian J. Sci. Eng.*, 2025, **50**(1), 41–63.
84 V. Tran, *et al.*, Layer-controlled band gap and anisotropic excitons in few-layer black phosphorus, *Phys. Rev. B: Condens. Matter Mater. Phys.*, 2014, **89**(23), 235319.
85 L. Y. Y. Li, G. J. Ye, Q. Ge, X. Ou, H. Wu, D. Feng, X. H. Chen and Y. Zhang, Black phosphorus field-effect transistors, *Nat. Nanotechnol.*, 2014, **9**, 372–377.
86 M. Buscema, *et al.*, Fast and broadband photoresponse of few-layer black phosphorus field-effect transistors, *Nano Lett.*, 2014, **14**(6), 3347–3352.
87 J. Qiao, *et al.*, High-mobility transport anisotropy and linear dichroism in few-layer black phosphorus, *Nat. Commun.*, 2014, **5**(1), 4475.
88 F. Withers, *et al.*, Light-emitting diodes by band-structure engineering in van der Waals heterostructures, *Nat. Mater.*, 2015, **14**(3), 301–306.
89 X. Ren, *et al.*, Environmentally robust black phosphorus nanosheets in solution: application for self–powered photodetector, *Adv. Funct. Mater.*, 2017, **27**(18), 1606834.
90 X. Ling, *et al.*, The renaissance of black phosphorus, *Proc. Natl. Acad. Sci. U. S. A.*, 2015, **112**(15), 4523–4530.
91 Y. Xu, *et al.*, Recent progress in black phosphorus and black-phosphorus-analogue materials: properties, synthesis and applications, *Nanoscale*, 2019, **11**(31), 14491–14527.
92 D. A. Bandurin, *et al.*, High electron mobility, quantum Hall effect and anomalous optical response in atomically thin InSe, *Nat. Nanotechnol.*, 2017, **12**(3), 223–227.
93 M. W. Zulfiqar, *et al.*, Gate-Controlled InSe/PtS_2 van der Waals Heterostructures for High-Performance Electronic and Optoelectronic Devices, *ACS Appl. Electron. Mater.*, 2024, **6**(11), 7906–7914.
94 C.-H. Ho, Thickness-dependent carrier transport and optically enhanced transconductance gain in III-VI multilayer InSe, *2D Mater.*, 2016, **3**(2), 025019.
95 J. F. Sánchez-Royo, *et al.*, Electronic structure, optical properties, and lattice dynamics in atomically thin indium selenide flakes, *Nano Res.*, 2014, **7**, 1556–1568.
96 S. Zhao, *et al.*, Highly polarized and fast photoresponse of black phosphorus–InSe vertical p–n heterojunctions, *Adv. Funct. Mater.*, 2018, **28**(34), 1802011.
97 Y. Yan, *et al.*, Self–Driven High Performance Broadband Photodetector Based on SnSe/InSe van der Waals Heterojunction, *Adv. Mater. Interfaces*, 2022, **9**(12), 2102068.
98 M. Yüksek, *et al.*, Nonlinear and saturable absorption characteristics of Ho doped InSe crystals, *Opt. Commun.*, 2014, **310**, 100–103.
99 Y. Pan, *et al.*, Strong in-plane optical and electrical anisotropies of multilayered γ-InSe for high-responsivity polarization-sensitive photodetectors, *ACS Appl. Mater. Interfaces*, 2022, **14**(18), 21383–21391.
100 D. Golberg, *et al.*, Boron nitride nanotubes, *Adv. Mater.*, 2007, **19**(18), 2413–2432.
101 S. Manzeli, *et al.*, 2D transition metal dichalcogenides, *Nat. Rev. Mater.*, 2017, **2**(8), 1–15.
102 W. Choi, *et al.*, Recent development of two-dimensional transition metal dichalcogenides and their applications, *Mater. Today*, 2017, **20**(3), 116–130.
103 J. A. Wilson, F. D. Salvo and S. Mahajan, Charge-density waves and superlattices in the metallic layered transition metal dichalcogenides, *Adv. Phys.*, 1975, **24**(2), 117–201.
104 A. Castellanos-Gomez, *et al.*, Isolation and characterization of few-layer black phosphorus, *2D Mater.*, 2014, **1**(2), 025001.
105 D. A. Bandurin, *et al.*, High electron mobility, quantum Hall effect and anomalous optical response in atomically thin InSe, *Nat. Nanotechnol.*, 2017, **12**(3), 223–227.
106 G. Han, *et al.*, Indium Selenides: Structural Characteristics, Synthesis and Their Thermoelectric Performances, *Small*, 2014, **10**(14), 2747–2765.
107 Q. H. Wang, *et al.*, Electronics and optoelectronics of two-dimensional transition metal dichalcogenides, *Nat. Nanotechnol.*, 2012, **7**(11), 699–712.
108 X. Yu, *et al.*, Atomically thin noble metal dichalcogenide: a broadband mid-infrared semiconductor, *Nat. Commun.*, 2018, **9**(1), 1545.
109 W. L. Chow, *et al.*, High mobility 2D palladium diselenide field–effect transistors with tunable ambipolar characteristics, *Adv. Mater.*, 2017, **29**(21), 1602969.
110 A. D. Oyedele, *et al.*, $PdSe_2$: pentagonal two-dimensional layers with high air stability for electronics, *J. Am. Chem. Soc.*, 2017, **139**(40), 14090–14097.
111 Y. Zhao, *et al.*, Extraordinarily Strong Interlayer Interaction in 2D Layered PtS_2, *Adv. Mater.*, 2016, **28**(12), 2399–2407.
112 J. Sun, *et al.*, Electronic, transport, and optical properties of bulk and mono-layer $PdSe_2$, *Appl. Phys. Lett.*, 2015, **107**(15), 153902-1–153902-4.
113 R. Lv, *et al.*, Transition metal dichalcogenides and beyond: synthesis, properties, and applications of single- and few-layer nanosheets, *Acc. Chem. Res.*, 2015, **48**(1), 56–64.
114 X. Duan, *et al.*, Two-dimensional transition metal dichalcogenides as atomically thin semiconductors: opportu-

nities and challenges, *Chem. Soc. Rev.*, 2015, **44**(24), 8859–8876.
115 P. Miró, M. Ghorbani-Asl and T. Heine, Two dimensional materials beyond MoS_2: noble–transition–metal dichalcogenides, *Angew. Chem., Int. Ed.*, 2014, **53**(11), 3015–3018.
116 A. B. Kaul, Two-dimensional layered materials: Structure, properties, and prospects for device applications, *J. Mater. Res.*, 2014, **29**(3), 348–361.
117 H. L. Zhuang and R. G. Hennig, Computational search for single-layer transition-metal dichalcogenide photocatalysts, *J. Phys. Chem. C*, 2013, **117**(40), 20440–20445.
118 M. Chhowalla, *et al.*, The chemistry of two-dimensional layered transition metal dichalcogenide nanosheets, *Nat. Chem.*, 2013, **5**(4), 263–275.
119 S. Lebègue, *et al.*, Two-dimensional materials from data filtering and ab initio calculations, *Phys. Rev. X*, 2013, **3**(3), 031002.
120 C.-H. Liu, *et al.*, Graphene photodetectors with ultrabroadband and high responsivity at room temperature, *Nat. Nanotechnol.*, 2014, **9**(4), 273–278.
121 X. Wang, *et al.*, High-responsivity graphene/silicon-heterostructure waveguide photodetectors, *Nat. Photonics*, 2013, **7**(11), 888–891.
122 G. X. Liang, *et al.*, Self–powered broadband kesterite photodetector with ultrahigh specific detectivity for weak light applications, *SusMat*, 2023, **3**(5), 682–696.
123 B. Mallampati, *et al.*, Role of surface in high photoconductive gain measured in ZnO nanowire-based photodetector, *J. Nanopart. Res.*, 2015, **17**, 1–10.
124 H. Wang, *et al.*, Approaching the external quantum efficiency limit in 2D photovoltaic devices, *Adv. Mater.*, 2022, **34**(39), 2206122.
125 L. Li, *et al.*, Chemical vapor deposition-grown nonlayered α-MnTe nanosheet for photodetectors with ultrahigh responsivity and external quantum efficiency, *Chem. Mater.*, 2020, **33**(1), 338–346.
126 V. Mackowiak, *et al.*, *NEP–noise equivalent power*. Thorlabs, Inc., 2015, pp. 56.
127 L. Huang, *et al.*, Infrared black phosphorus phototransistor with tunable responsivity and low noise equivalent power, *ACS Appl. Mater. Interfaces*, 2017, **9**(41), 36130–36136.
128 L. Li, *et al.*, Quantum oscillations in a two-dimensional electron gas in black phosphorus thin films, *Nat. Nanotechnol.*, 2015, **10**(7), 608–613.
129 C. Chen, *et al.*, Three-dimensional integration of black phosphorus photodetector with silicon photonics and nanoplasmonics, *Nano Lett.*, 2017, **17**(2), 985–991.
130 L. Huang, *et al.*, Waveguide-Integrated Black Phosphorus Photodetector for Mid-Infrared Applications, *ACS Nano*, 2019, **13**(1), 913–921.
131 L. Li, *et al.*, Black phosphorus field-effect transistors, *Nat. Nanotechnol.*, 2014, **9**(5), 372–377.
132 Q. F. Li, *et al.*, Theoretical prediction of high carrier mobility in single-walled black phosphorus nanotubes, *Appl. Surf. Sci.*, 2018, **441**, 1079–1085.
133 Y. Liu, *et al.*, Highly Efficient and Air-Stable Infrared Photodetector Based on 2D Layered Graphene–Black Phosphorus Heterostructure, *ACS Appl. Mater. Interfaces*, 2017, **9**(41), 36137–36145.
134 F. Bonaccorso, *et al.*, Graphene photonics and optoelectronics, *Nat. Photonics*, 2010, **4**(9), 611–622.
135 M. Buscema, *et al.*, Fast and broadband photoresponse of few-layer black phosphorus field-effect transistors, *Nano Lett.*, 2014, **14**(6), 3347–3352.
136 L. Zhang, *et al.*, Synthesis Techniques, Optoelectronic Properties, and Broadband Photodetection of Thin–Film Black Phosphorus, *Adv. Opt. Mater.*, 2020, **8**(15), 2000045.
137 C. Hou, *et al.*, Multilayer black phosphorus near-infrared photodetectors, *Sensors*, 2018, **18**(6), 1668.
138 F. Xia, H. Wang and Y. Jia, Rediscovering black phosphorus as an anisotropic layered material for optoelectronics and electronics, *Nat. Commun.*, 2014, **5**(1), 4458.
139 J. Heo, *et al.*, Reconfigurable van der Waals heterostructured devices with metal–insulator transition, *Nano Lett.*, 2016, **16**(11), 6746–6754.
140 H. Qiao, *et al.*, Broadband photodetectors based on graphene–Bi_2Te_3 heterostructure, *ACS Nano*, 2015, **9**(2), 1886–1894.
141 N. Perea-López, *et al.*, Photosensor device based on few–layered WS_2 films, *Adv. Funct. Mater.*, 2013, **23**(44), 5511–5517.
142 L. Tang, *et al.*, Deep ultraviolet to near-infrared emission and photoresponse in layered N-doped graphene quantum dots, *ACS Nano*, 2014, **8**(6), 6312–6320.
143 C. Lan, *et al.*, Highly responsive and broadband photodetectors based on WS 2-graphene van der Waals epitaxial heterostructures, *J. Mater. Chem. C*, 2017, **5**(6), 1494–1500.
144 L. Vicarelli, *et al.*, Graphene field-effect transistors as room-temperature terahertz detectors, *Nat. Mater.*, 2012, **11**(10), 865–871.
145 B. Y. Zhang, *et al.*, Broadband high photoresponse from pure monolayer graphene photodetector, *Nat. Commun.*, 2013, **4**(1), 1811.
146 W. C. Tan, *et al.*, A black phosphorus carbide infrared phototransistor, *Adv. Mater.*, 2018, **30**(6), 1705039.
147 P. Hu, *et al.*, Highly sensitive phototransistors based on two-dimensional GaTe nanosheets with direct bandgap, *Nano Res.*, 2014, **7**, 694–703.
148 D. Zhang, *et al.*, Understanding charge transfer at pbs–decorated graphene surfaces toward a tunable photosensor, *Adv. Mater.*, 2012, **24**(20), 2715–2720.
149 X. Zhou, *et al.*, Tunneling diode based on WSe_2/SnS_2 heterostructure incorporating high detectivity and responsivity, *Adv. Mater.*, 2018, **30**(7), 1703286.
150 S.-H. Jo, *et al.*, Broad Detection Range Rhenium Diselenide Photodetector Enhanced by (3-Aminopropyl) Triethoxysilane and Triphenylphosphine Treatment, *Adv. Mater.*, 2016, **28**(31), 6711–6718.
151 B. Chitara, *et al.*, Infrared photodetectors based on reduced graphene oxide and graphene nanoribbons, *Adv. Mater.*, 2011, **23**(45), 5419.

152 Y. Chen, *et al.*, High–performance photovoltaic detector based on $MoTe_2/MoS_2$ van der Waals heterostructure, *Small*, 2018, **14**(9), 1703293.
153 T. Echtermeyer, *et al.*, Strong plasmonic enhancement of photovoltage in graphene, *Nat. Commun.*, 2011, **2**(1), 458.
154 M. E. Itkis, *et al.*, Enhanced photosensitivity of electro-oxidized epitaxial graphene, *Appl. Phys. Lett.*, 2011, **98**(9), 093115-1–093115-3.
155 W. Luo, *et al.*, Gate tuning of high–performance InSe–based photodetectors using graphene electrodes, *Adv. Opt. Mater.*, 2015, **3**(10), 1418–1423.
156 Q. Guo, *et al.*, Black phosphorus mid-infrared photodetectors with high gain, *Nano Lett.*, 2016, **16**(7), 4648–4655.
157 X. Chen, *et al.*, Widely tunable black phosphorus mid-infrared photodetector, *Nat. Commun.*, 2017, **8**(1), 1672.
158 Q. A. Vu, *et al.*, Tuning Carrier Tunneling in van der Waals Heterostructures for Ultrahigh Detectivity, *Nano Lett.*, 2017, **17**(1), 453–459.
159 F. Liu, *et al.*, Highly sensitive detection of polarized light using anisotropic 2D ReS_2, *Adv. Funct. Mater.*, 2016, **26**(8), 1169–1177.
160 M. Mittendorff, *et al.*, Ultrafast graphene-based broadband THz detector, *Appl. Phys. Lett.*, 2013, **103**(2), 021113-1–021113-4.
161 W. Guo, *et al.*, Oxygen–assisted charge transfer between ZnO quantum dots and graphene, *Small*, 2013, **9**(18), 3031–3036.
162 W. Choi, *et al.*, High–detectivity multilayer MoS_2 phototransistors with spectral response from ultraviolet to infrared, *Adv. Mater.*, 2012, **24**(43), 5832.
163 W. J. Yu, *et al.*, Unusually efficient photocurrent extraction in monolayer van der Waals heterostructure by tunnelling through discretized barriers, *Nat. Commun.*, 2016, **7**(1), 13278.
164 P. Hu, *et al.*, Synthesis of few-layer GaSe nanosheets for high performance photodetectors, *ACS Nano*, 2012, **6**(7), 5988–5994.
165 T. Jiang, *et al.*, Broadband High–Responsivity Photodetectors Based on Large–Scale Topological Crystalline Insulator SnTe Ultrathin Film Grown by Molecular Beam Epitaxy, *Adv. Opt. Mater.*, 2017, **5**(5), 1600727.
166 M. Amani, *et al.*, Mid-wave infrared photoconductors based on black phosphorus-arsenic alloys, *ACS Nano*, 2017, **11**(11), 11724–11731.
167 F. Xia, *et al.*, Ultrafast graphene photodetector, *Nat. Nanotechnol.*, 2009, **4**(12), 839–843.
168 J. Wu, *et al.*, Colossal ultraviolet photoresponsivity of few-layer black phosphorus, *ACS Nano*, 2015, **9**(8), 8070–8077.
169 C. O. Kim, *et al.*, High photoresponsivity in an all-graphene p–n vertical junction photodetector, *Nat. Commun.*, 2014, **5**(1), 3249.
170 Y. Liu, *et al.*, Plasmon resonance enhanced multicolour photodetection by graphene, *Nat. Commun.*, 2011, **2**(1), 579.
171 K. Zhang, *et al.*, Ultrasensitive near-infrared photodetectors based on a graphene–$MoTe_2$–graphene vertical van der Waals heterostructure, *ACS Appl. Mater. Interfaces*, 2017, **9**(6), 5392–5398.
172 M. Freitag, *et al.*, Photocurrent in graphene harnessed by tunable intrinsic plasmons, *Nat. Commun.*, 2013, **4**(1), 1951.
173 A. M. Afzal, *et al.*, High-Performance p-BP/n-$PdSe_2$ Near-Infrared Photodiodes with a Fast and Gate-Tunable Photoresponse, *ACS Appl. Mater. Interfaces*, 2020, **12**(17), 19625–19634.
174 J. Yao, *et al.*, Ultra-broadband and high response of the Bi 2 Te 3−Si heterojunction and its application as a photodetector at room temperature in harsh working environments, *Nanoscale*, 2015, **7**(29), 12535–12541.
175 D.-S. Tsai, *et al.*, Few-layer MoS_2 with high broadband photogain and fast optical switching for use in harsh environments, *ACS Nano*, 2013, **7**(5), 3905–3911.
176 Y. Tao, *et al.*, Flexible photodetector from ultraviolet to near infrared based on a SnS 2 nanosheet microsphere film, *J. Mater. Chem. C*, 2015, **3**(6), 1347–1353.
177 H. Yuan, *et al.*, Polarization-sensitive broadband photodetector using a black phosphorus vertical p–n junction, *Nat. Nanotechnol.*, 2015, **10**(8), 707–713.
178 R. Cheng, *et al.*, Electroluminescence and photocurrent generation from atomically sharp WSe_2/MoS_2 heterojunction p–n diodes, *Nano Lett.*, 2014, **14**(10), 5590–5597.
179 A. Gao, *et al.*, Observation of ballistic avalanche phenomena in nanoscale vertical InSe/BP heterostructures, *Nat. Nanotechnol.*, 2019, **14**(3), 217–222.
180 R. H. Hadfield, Single-photon detectors for optical quantum information applications, *Nat. Photonics*, 2009, **3**(12), 696–705.
181 G. Zhao, *et al.*, Mobile lidar system for environmental monitoring, *Appl. Opt.*, 2017, **56**(5), 1506–1516.
182 Q. Tang, *et al.*, Infrared Photodetection from 2D/3D van der Waals Heterostructures, *Nanomaterials*, 2023, **13**(7), 1169.
183 R. Cao, *et al.*, Black Phosphorous/Indium Selenide Photoconductive Detector for Visible and Near-Infrared Light with High Sensitivity, *Adv. Opt. Mater.*, 2019, **7**(12), 1900020.
184 C. Du, *et al.*, High responsivity and broadband polarized photodetectors based on InSe/$ReSe_2$ van der Waals heterostructures, *J. Alloys Compd.*, 2022, **919**, 165586.
185 K. K. Manga, *et al.*, High–performance broadband photodetector using solution–processible PbSe–TiO_2–graphene hybrids, *Adv. Mater.*, 2012, **24**(13), 1697.
186 D. Schall, *et al.*, 50 GBit/s photodetectors based on wafer-scale graphene for integrated silicon photonic communication systems, *ACS Photonics*, 2014, **1**(9), 781–784.
187 A. Urich, K. Unterrainer and T. Mueller, Intrinsic response time of graphene photodetectors, *Nano Lett.*, 2011, **11**(7), 2804–2808.
188 J. Mao, *et al.*, Ultrafast, broadband photodetector based on $MoSe_2$/silicon heterojunction with vertically standing

layered structure using graphene as transparent electrode, *Adv. Sci.*, 2016, **3**(11), 1600018.
189 N. Youngblood, *et al.*, Waveguide-integrated black phosphorus photodetector with high responsivity and low dark current, *Nat. Photonics*, 2015, **9**(4), 247–252.
190 D. Sun, *et al.*, Ultrafast hot-carrier-dominated photocurrent in graphene, *Nat. Nanotechnol.*, 2012, **7**(2), 114.
191 Y. Kang, *et al.*, Monolithic germanium/silicon avalanche photodiodes with 340 GHz gain–bandwidth product, *Nat. Photonics*, 2009, **3**(1), 59–63.
192 X. Gan, *et al.*, Chip-integrated ultrafast graphene photodetector with high responsivity, *Nat. Photonics*, 2013, **7**(11), 883–887.
193 C. Zhao, *et al.*, Highly efficient 1D p-Te/2D n-Bi_2Te_3 heterojunction self-driven broadband photodetector, *Nano Res.*, 2024, **17**(3), 1864–1874.
194 L. Zhang, *et al.*, Structure and properties of violet phosphorus and its phosphorene exfoliation, *Angew. Chem.*, 2020, **132**(3), 1090–1096.
195 D. Wu, *et al.*, Fabrication of 2D $PdSe_2$/3D CdTe Mixed-Dimensional van der Waals Heterojunction for Broadband Infrared Detection, *ACS Appl. Mater. Interfaces*, 2021, **13**(35), 41791–41801.
196 C. H. Lee, *et al.*, Design of p-WSe_2/n-Ge Heterojunctions for High-Speed Broadband Photodetectors, *Adv. Funct. Mater.*, 2022, **32**(4), 2107992.
197 W. Ahmad, *et al.*, Ultrasensitive Near-Infrared Polarization Photodetectors with Violet Phosphorus/InSe van der Waals Heterostructures, *ACS Appl. Mater. Interfaces*, 2024, **16**(15), 19214–19224.
198 P. Xiao, *et al.*, Solution-Processed 3D RGO–MoS_2/Pyramid Si Heterojunction for Ultrahigh Detectivity and Ultra-Broadband Photodetection, *Adv. Mater.*, 2018, **30**(31), 1801729.
199 Z. Wang, *et al.*, High-responsivity graphene/hyperdoped-silicon heterostructure infrared photodetectors, *Opt. Laser Technol.*, 2022, **153**, 108291.
200 S. Gao, *et al.*, Graphene/MoS_2/Graphene Vertical Heterostructure–Based Broadband Photodetector with High Performance, *Adv. Mater. Interfaces*, 2021, **8**(3), 2001730.
201 Z. Wang, *et al.*, Construction of mixed-dimensional WS 2/Si heterojunctions for high-performance infrared photodetection and imaging applications, *J. Mater. Chem. C*, 2020, **8**(20), 6877–6882.
202 D. Wu, *et al.*, Mixed-dimensional PdSe 2/SiNWA heterostructure based photovoltaic detectors for self-driven, broadband photodetection, infrared imaging and humidity sensing, *J. Mater. Chem. A*, 2020, **8**(7), 3632–3642.
203 M. Long, *et al.*, Room temperature high-detectivity mid-infrared photodetectors based on black arsenic phosphorus, *Sci. Adv.*, 2017, **3**(6), e1700589.
204 L. Zeng, *et al.*, van der Waals epitaxial growth of mosaic–like 2D platinum ditelluride layers for room–temperature mid–infrared photodetection up to 10.6 μm, *Adv. Mater.*, 2020, **32**(52), 2004412.
205 R. Cao, *et al.*, Black phosphorous/indium selenide photoconductive detector for visible and near–infrared light with high sensitivity, *Adv. Opt. Mater.*, 2019, **7**(12), 1900020.
206 F. Liang, *et al.*, Ferromagnetic CoSe broadband photodetector at room temperature, *Nanotechnology*, 2020, **31**(37), 374002.
207 L. Viti, *et al.*, Thermoelectric graphene photodetectors with sub-nanosecond response times at terahertz frequencies, *Nanophotonics*, 2020, **10**(1), 89–98.
208 C. Shen, *et al.*, Tellurene photodetector with high gain and wide bandwidth, *ACS Nano*, 2019, **14**(1), 303–310.
209 C. Yin, *et al.*, Ultrabroadband photodetectors up to 10.6 μm based on 2D Fe_3O_4 nanosheets, *Adv. Mater.*, 2020, **32**(25), 2002237.
210 X. W. Tong, *et al.*, Direct Tellurization of Pt to Synthesize 2D PtTe(2) for High-Performance Broadband Photodetectors and NIR Image Sensors, *ACS Appl. Mater. Interfaces*, 2020, **12**(48), 53921–53931.
211 L. Xie, *et al.*, An Atomically Thin Air–Stable Narrow–Gap Semiconductor Cr_2S_3 for Broadband Photodetection with High Responsivity, *Adv. Electron. Mater.*, 2021, **7**(7), 2000962.
212 F. Wang, *et al.*, Submillimeter 2D Bi_2Se_3 flakes toward high–performance infrared photodetection at optical communication wavelength, *Adv. Funct. Mater.*, 2018, **28**(33), 1802707.
213 J. O. Island, *et al.*, Gate controlled photocurrent generation mechanisms in high-gain In_2Se_3 phototransistors, *Nano Lett.*, 2015, **15**(12), 7853–7858.
214 M. Long, *et al.*, Broadband photovoltaic detectors based on an atomically thin heterostructure, *Nano Lett.*, 2016, **16**(4), 2254–2259.
215 D. Kufer, *et al.*, Hybrid 2D-0D MoS_2-PbS quantum dot photodetectors, *Adv. Mater.*, 2014, **27**(1), 176–180.
216 W. Feng, *et al.*, Ultrahigh photo-responsivity and detectivity in multilayer InSe nanosheets phototransistors with broadband response, *J. Mater. Chem. C*, 2015, **3**(27), 7022–7028.
217 Q. A. Vu, *et al.*, Tuning carrier tunneling in van der Waals heterostructures for ultrahigh detectivity, *Nano Lett.*, 2017, **17**(1), 453–459.
218 L. Wang, *et al.*, MoS_2/Si heterojunction with vertically standing layered structure for ultrafast, high–detectivity, self–driven visible–near infrared photodetectors, *Adv. Funct. Mater.*, 2015, **25**(19), 2910–2919.
219 W. Zhang, *et al.*, Role of metal contacts in high-performance phototransistors based on WSe_2 monolayers, *ACS Nano*, 2014, **8**(8), 8653–8661.
220 S. Zhang, *et al.*, Black Arsenic Phosphorus Mid-Wave Infrared Barrier Detector with High Detectivity at Room Temperature, *Adv. Mater.*, 2024, **36**(21), 2313134.
221 A. Chaves, *et al.*, Bandgap engineering of two-dimensional semiconductor materials, *npj 2D Mater. Appl.*, 2020, **4**(1), 29.
222 X. Yao, *et al.*, Thickness-dependent bandgap of transition metal dichalcogenides dominated by interlayer van der Waals interaction, *Phys. E*, 2019, **109**, 11–16.

223 S. Susarla, *et al.*, Quaternary 2D Transition Metal Dichalcogenides (TMDs) with Tunable Bandgap, *Adv. Mater.*, 2017, **29**(35), 1702457.
224 E. Sousa, *et al.*, A review on the application of medical infrared thermal imaging in hands, *Infrared Phys. Technol.*, 2017, **85**, 315–323.
225 N. Li, *et al.*, Organic Upconversion Imager with Dual Electronic and Optical Readouts for Shortwave Infrared Light Detection, *Adv. Funct. Mater.*, 2021, **31**(16), 2100565.
226 T. Yokota, *et al.*, A conformable imager for biometric authentication and vital sign measurement, *Nat. Electron.*, 2020, **3**(2), 113–121.
227 C. D. Tran, *Infrared multispectral imaging: principles and instrumentation*, 2003.
228 M. Rabeel, *et al.*, Eco-friendly wide-spectrum flexible photo-responsive polymer nanocomposite based on ZnO/cellulose nanofiber, *Appl. Mater. Today*, 2024, **41**, 102508.
229 X. Tang, *et al.*, Dual-band infrared imaging using stacked colloidal quantum dot photodiodes, *Nat. Photonics*, 2019, **13**(4), 277–282.
230 X. Tang, *et al.*, Towards Infrared Electronic Eyes: Flexible Colloidal Quantum Dot Photovoltaic Detectors Enhanced by Resonant Cavity, *Small*, 2019, **15**(12), 1804920.
231 J. Yin, *et al.*, Selectively enhanced photocurrent generation in twisted bilayer graphene with van Hove singularity, *Nat. Commun.*, 2016, **7**(1), 10699.
232 K. F. Mak and J. Shan, Photonics and optoelectronics of 2D semiconductor transition metal dichalcogenides, *Nat. Photonics*, 2016, **10**(4), 216–226.
233 J. Yin, *et al.*, Ultrafast and highly sensitive infrared photodetectors based on two-dimensional oxyselenide crystals, *Nat. Commun.*, 2018, **9**(1), 3311.
234 J. Wu, *et al.*, High electron mobility and quantum oscillations in non-encapsulated ultrathin semiconducting Bi_2O_2Se, *Nat. Nanotechnol.*, 2017, **12**(6), 530–534.
235 N. Gabor, *et al.*, *Ultrafast photocurrent measurement of the escape time of electrons and holes from carbon nanotube pin photodiodes*, 2012.
236 D. H. Lee, *et al.*, Self-Assembled Monolayer Doping for $MoTe_2$ Field-Effect Transistors: Overcoming PN Doping Challenges in Transition Metal Dichalcogenides, *ACS Appl. Mater. Interfaces*, 2023, **15**(44), 51518–51526.
237 W. Yu, *et al.*, Near–infrared photodetectors based on $MoTe_2$/graphene heterostructure with high responsivity and flexibility, *Small*, 2017, **13**(24), 1700268.
238 A. Li, *et al.*, Ultrahigh-Sensitive Broadband Photodetectors Based on Dielectric Shielded $MoTe_2$/Graphene/SnS_2 p–g–n Junctions, *Adv. Mater.*, 2019, **31**(6), 1805656.
239 A. Rogalski, M. Kopytko and P. Martyniuk, Two-dimensional infrared and terahertz detectors: Outlook and status, *Appl. Phys. Rev.*, 2019, **6**(2), 021316.
240 R. Lewis, A review of terahertz detectors, *J. Phys. D: Appl. Phys.*, 2019, **52**(43), 433001.
241 A. Castellanos-Gomez, *et al.*, van der Waals heterostructures, *Nat. Rev. Methods Primers*, 2022, **2**(1), 58.
242 T. Chowdhury, E. C. Sadler and T. J. Kempa, Progress and prospects in transition-metal dichalcogenide research beyond 2D, *Chem. Rev.*, 2020, **120**(22), 12563–12591.
243 Y. Fang, *et al.*, Mid–infrared photonics using 2D materials: status and challenges, *Laser Photonics Rev.*, 2020, **14**(1), 1900098.
244 R. Avrahamy, *et al.*, Chalcogenide-based, all-dielectric, ultrathin metamaterials with perfect, incidence-angle sensitive, mid-infrared absorption: inverse design, analysis, and applications, *Nanoscale*, 2021, **13**(26), 11455–11469.
245 S. Chakravarty, *et al.*, Hybrid material integration in silicon photonic integrated circuits, *J. Semicond.*, 2021, **42**(4), 041303.
246 M. He, *et al.*, Guided Mid–IR and Near–IR Light within a Hybrid Hyperbolic–Material/Silicon Waveguide Heterostructure, *Adv. Mater.*, 2021, **33**(11), 2004305.
247 V. Kammar, *et al.*, Light trap: a dynamic tool for data analysis, documenting, and monitoring insect populations and diversity, Innovative pest management approaches for the 21st century: harnessing automated unmanned technologies, 2020, pp. 137–163.
248 E. S. Penev, N. Marzari and B. I. Yakobson, Theoretical prediction of two-dimensional materials, behavior, and properties, *ACS Nano*, 2021, **15**(4), 5959–5976.
249 S. Haastrup, *et al.*, The Computational 2D Materials Database: high-throughput modeling and discovery of atomically thin crystals, *2D Mater.*, 2018, **5**(4), 042002.
250 W. Zhou, *et al.*, Quantum-tuned cascade multijunction infrared photodetector, *ACS Nano*, 2023, **17**(19), 18864–18872.
251 P. Martyniuk, A. Rogalski and S. Krishna, Interband quantum cascade infrared photodetectors: Current status and future trends, *Phys. Rev. Appl.*, 2022, **17**(2), 027001.
252 S. Fan, *et al.*, Strategy for transferring van der Waals materials and heterostructures, *2D Mater.*, 2024, **11**(3), 033002.
253 Y. Zhao, *et al.*, Large-area transfer of two-dimensional materials free of cracks, contamination and wrinkles via controllable conformal contact, *Nat. Commun.*, 2022, **13**(1), 4409.
254 Y. Huang, *et al.*, Hybrid superlattices of two-dimensional materials and organics, *Chem. Soc. Rev.*, 2020, **49**(19), 6866–6883.
255 M. R. Islam, S. Afroj and N. Karim, Scalable Production of 2D Material Heterostructure Textiles for High-Performance Wearable Supercapacitors, *ACS Nano*, 2023, **17**(18), 18481–18493.
256 T. H. Choudhury, *et al.**,, *Scalable synthesis of 2D materials, in 2D Materials for Electronics, Sensors and Devices*, 2023, pp. 1–54.
257 E. Pascual, *et al.*, Electronic transport and noise characterization in MoS_2, *Semicond. Sci. Technol.*, 2020, **35**(5), 055021.
258 A. A. Balandin, E. Paladino and P. J. Hakonen, Electronic noise—From advanced materials to quantum technologies, *Appl. Phys. Lett.*, 2024, **124**(5), 050401-1–050401-4.